

UC Davis

UC Davis Electronic Theses and Dissertations

Title

Radiation-Pattern-Effects in Bay Area Ground-Motion Models

Permalink

<https://escholarship.org/uc/item/7g45t2xh>

Author

Liou, Irene Yung-Wen

Publication Date

2022

Peer reviewed|Thesis/dissertation

Radiation-Pattern-Effects
in
Bay Area Ground-Motion Models

By

IRENE Y. LIOU
THESIS

Submitted in partial satisfaction of the requirements for the degree of

MASTER OF SCIENCE

in

Civil and Environmental Engineering

in the

OFFICE OF GRADUATE STUDIES

of the

UNIVERSITY OF CALIFORNIA

DAVIS

Approved:

Norman Abrahamson, Chair

Katerina Ziotopoulou

Boris Jeremic

Committee in Charge

2022

Radiation-Pattern-Effects in Bay Area Ground-Motion Models

Irene Liou ^{*1} and Norman Abrahamson^{†1}

¹Department of Civil and Environmental Engineering, University of
California, Davis

*yliou@davis.edu

†abrahamson@berkeley.edu

Abstract

Ground-motions from 14 well-recorded moderate magnitude (M3.0 - M4.9) Bay Area earthquakes were compared to predictions from Ergodic Ground-Motion Models (GMMs). The radiation pattern is part of the earthquake source, however, in current GMMs the radiation pattern is not modeled explicitly and is treated as part of the path term in the regression. Without the proper separation between the earthquake source parameters and path parameters, the true path effect can be obscured. Going forward, the radiation pattern should be removed from the path effect in GMMs and included as part of the anisotropic source term for moderate earthquakes. This can isolate the 3-D crustal structure path effects from the radiation-pattern-effects and the radiation-pattern-corrected residuals can be used for evaluations and calibration of 3-D simulations.

Introduction

The development of ground-motion models (GMMs) — referred to in past literature as attenuation relations or Ground-Motion Prediction Equations (GMPEs) — has spanned a decades-long journey of improving shaking predictions for future earthquake scenarios. GMMs, usually used for estimating Pseudo Spectral Accelerations (PSAs), provide crucial earthquake ground-motions for a broad spectrum of seismic safety analyses ranging from Probabilistic Seismic Hazard Analysis (PSHAs) to structural response evaluations. In efforts to improve modeling accuracy, approaches to GMMs and input parameters have evolved over time. Empirical GMMs have consistently included parameters of earthquake magnitude, site-to-source distance, and the local site condition; however, between models, there have been variations in how these parameters are precisely characterized (Abrahamson 2008).

A key, unchanging consideration of GMMs is the inherent variability of earthquake ground-motions. A wide variety of shaking intensities can result from an earthquake of singular magnitude. In other words, the expected ground-motion of an earthquake scenario is represented by a distribution, which has a median and a standard deviation. Ground-motion is an aleatory variable since the shaking intensity lacks a specified single value given the simplified descriptions of the source, path, and site used in the GMMs. Aleatory variability arises from the modeling simplifications used in the GMMs. Though earthquakes are caused by a physical process, due to limitations in earthquake science, simplified earthquake models are used. Simplified models lead to variations as a consequence of simple parameterization. For example, an earthquake's source is not fully explained by an earthquake's magnitude and rupture dimensions. Since this simple parameterization of magnitude and fault rupture inputs cannot fully explain all

observations, the differences are classified as randomness within the construct of the model even though there is a physical cause behind the variation. In contrast, epistemic uncertainty refers to uncertainty in the simplified models. Due to limited information, there is uncertainty that the results in the simplified model — such as the median and standard deviation for a given scenario — are correct for the context of the simplified model. Though the model is not fully correct, given that it is a simplified version of an earthquake process, there is uncertainty that this is the best version of this simplified model.

The distinction between epistemic uncertainty and aleatory variability is a non-absolute parameterization that can change depending on the simplification used in the GMM. An example of this is exhibited through an overview of basic GMMs introduced in order of progressively smaller aleatory terms by incrementally identifying effects and adding repeatable terms into the GMM.

Al Atik et al. (2010) use the following equation to describe Ergodic GMMs:

$$Y_{es} = f(M, R, V_{S30}, \dots) + \delta_{es} \quad (1)$$

$$\delta_{es} = \delta B_e + \delta W_{es} \quad (2)$$

where Y_{es} is the observed ground-motion on a log scale resulting from an earthquake e at a particular station s . The $f(M, R, V_{S30}, \dots)$ term is the median ground-motion predicted typically from a global or regional model that combines broad tectonic categories. It is a function of variables including magnitude M , source-to-station distance R , and the time-averaged shear-wave velocity in the top 30 meters V_{S30} . In Equation (2), δ_{es} is

the total residual difference between the GMM prediction and the recorded ground-motion comprised of aleatory terms δB_e and δW_{es} . δB_e is the between-event residual which shows the average difference between the recorded ground-motion from a specific earthquake e and the median prediction and has a corresponding standard deviation of τ (Figure 1). δW_{es} is the within-event residual, which represents the misfit between the recording at a particular seismic station s compared to the median ground-motion prediction for an earthquake e . W_{es} has a corresponding standard deviation of ϕ . In Equation (3) the total standard deviation is represented by:

$$\sigma = \sqrt{\tau^2 + \phi^2} \quad (3)$$

Ergodic GMMs, the most simplified model and approach due to its assumption that the same model applies to all sources and sites throughout the world, have the largest standard deviation and therefore the largest aleatory variability. In contrast, Non-Ergodic GMMs are the most site-specific and typically have the least aleatory variability and smallest standard deviation.

Partially Non-Ergodic models lie in between Ergodic and Non-Ergodic GMMs. They are more site-specific than Ergodic GMMs, however, less site-specific than Non-Ergodic GMMs. Using Equation (4), the aleatory term δW_{es} is decomposed into an epistemic site term of the site-to-site residual $\delta S_2 S_s$ and a smaller aleatory term of the within-site residual $\delta W S_{es}$:

$$\delta W_{es} = \delta S_2 S_s + \delta W S_{es} \quad (4)$$

$$Y_{es} = f(M, R, V_{S30}, \dots) + \delta B_e + \delta S2S_s + \delta W S_{es} \quad (5)$$

In the Partially Non-Ergodic model of Equation (5), site-to-site residual $\delta S2S_s$ describes the deviation from the average site response of a specific site to the average-site response predicted by GMMs for a particular V_{S30} . The within-site residual $\delta W S_{es}$ encompasses path variations as well as azimuthal variability influencing source, path, and site effects. $\delta S2S_s$ has a corresponding standard deviation of ϕ_{S2S} and the $\delta W S_{es}$ has a corresponding standard deviation of ϕ_{SS} that has the following relation shown in Equation (6):

$$\phi = \sqrt{\phi_{S2S}^2 + \phi_{SS}^2} \quad (6)$$

By including the $\delta S2S_s$ term, the model fits the data better and the aleatory variability is reduced to the single-station sigma value (σ_{SS}).

$$\sigma_{ss} = \sqrt{\tau^2 + \phi_{SS}^2} \quad (7)$$

This example of systematically splitting aleatory terms into smaller aleatory terms and epistemic terms shows how modeling parameterization can change what is classified as aleatory variability and epistemic uncertainty. However, once a modeling framework is established the distinction between epistemic and aleatory terms is fixed.

In the study by Kotha et al. (2019), the authors modified the parameterization of Partially Non-Ergodic GMMs from Equation (5) after finding a frequency-, distance-, and style-of-faulting dependency on anisotropic to isotropic transitioning shear-wave radiation-pattern-effects in active shallow crustal earthquake recordings from

the Japanese KiK-net strong-motion network and the NGA-West2 data set (Ancheta et al., 2014; Dawood et al., 2016). Radiation-pattern-effects capture azimuthal variations from radiated energy of the earthquake source. Though radiation pattern is a separate concept from directivity, the two are related. Directivity is a maximum amplitude on the radiation pattern node that occurs due to positive interference from approaching rupture waves. Radiation patterns are azimuthally dependent, however, they do not depend on approaching rupture waves. Their amplitudinal energy differences between nodal maxima and minima are dependent on the earthquake source and faulting geometry. An idealized and theoretical radiation pattern is completely anisotropic and deterministic. However, measured radiation patterns display characteristics in between anisotropic and isotropic. The analysis by Kotha et al. (2019) was focused on periods $T = 0.1$ s to 1 s. In Figures 2 and 3, the empirical ground-motions and theoretical ground-motions are in most agreement (in other words, the empirical ground-motion transitions from a stochastic process to a deterministic process) at larger periods. The study also shows through Figure 4 that the radiation-pattern-effect in strike-slip events at $T = 0.5$ s is significant up until 100 km. For longer periods ($T = 1$ s), the radiation-pattern-effect persists significantly up to 200 km. For normal and oblique-slip events, the radiation pattern decreases at much shorter distances of around 20-40 km.

Current GMMs have an oversimplified stochastic input and isotropic output. In order to introduce some anisotropy, the Equation (7) was proposed using a linear mixed effects regression:

$$\delta W S_{es} = s_0 + s_1 * A S_{es} \quad (8)$$

where s_0 is the y-intercept and the radiation pattern term δAS_{es} has a slope s_1 , representing the correlation between empirical and theoretical radiation pattern or the strength of the radiation pattern. Using these adjustment factors, ϕ (standard deviation of δWS_{es}) is reduced by 8% with up to $\pm 40\%$ variation from the average amplitude.

Since the authors saw a significant radiation-pattern-effect using their global data set, this motivated the investigation of the radiation-pattern-effect in the Bay Area ground-motions. The inclusion of radiation pattern was also useful in more accurately simulating peak ground accelerations (PGA) from the November 23rd, 1980 earthquake in southern Italy (Sirovich 1994). The author also suggested to include radiation pattern in ground-motion predictions.

Though the radiation-pattern-effect has been extensively studied in seismology, it has not been included in GMMs due to reasons such as inadequate sampling density of strong-motion to observe the radiation pattern for a single event and the complication that large earthquakes are not point sources with a single radiation pattern. The focus of the study, however, was intended to gain a better understanding of the path effect due to the 3-D crustal structure, which could potentially be clouded if the radiation-pattern-effect was significant. Similar to the study by Takemura et al. (2010) the radiation-pattern-effect was expected to be less visible and more stochastic at lower periods.

Data

Fourteen small-magnitude Bay Area earthquakes from M3.0 to M4.9 (shown in Figure 5) were selected due to the abundant amount of ground-motion data for small earthquakes

in comparison to ground-motion data for large earthquakes. The data set is listed in Table 1. For each earthquake, PSAs were obtained from the Strong Motion Center and the residuals were obtained relative to the Abrahamson et al. (2014) (ASK14) GMM. Ergodic GMMs from Equation (1) were used instead of the Partially-Non Ergodic GMMs from Equation (4) since the earthquakes analyzed are from a small region, resulting in similar ray paths that can lead to a trade-off between the site term and the path term. Since most of the well-recorded moderate Bay Area earthquakes found in the Strong-Motion database originated from the Hayward fault — with only a few other earthquakes from other fault systems — the range of crustal sampling and ray paths currently may not be wide enough for a more site-specific interpretation, therefore with the current data set, the simplest GMM is the most appropriate.

Estimation of Radiation Pattern

GMMs are based on peak amplitudes, which are controlled by the S-waves. Similarly to the paper by Kotha et al. (2019), S-wave radiation patterns were investigated since S-waves are the strongest and most damaging seismic waves. As noted by Kotha et al. (2019), explicitly modeling the radiation pattern in seismic hazard assessments is generally excluded and GMMs assume that the S-wave radiation pattern is isotropic. Radiation pattern, however, is not truly isotropic. It is strongly azimuthally-dependent. The effect of radiation pattern has strong potential for changing the ground-motion amplitude significantly (Boore et al. 2006).

The radiation pattern is dependent on earthquake wave type (e.g., SH and SV), the strike, slip, dip, take-off angle at the source, and station azimuth. The S-wave

radiation pattern was calculated based on earthquake faulting geometry of fault strike, dip (δ) and rake (λ) from the USGS catalog. The ϕ indicates fault strike subtracted by the station's azimuth and i_h is the take-off angle. The program TauP was used to calculate take-off angles, and the USGS 3-D model for the Bay Area was used to estimate the velocity profile at each station (Brocher et al., 2006; Crotwell et al., 1999). The horizontal R^{SH} and vertical R^{SV} radiation components were calculated for each station recording of all earthquakes using Equation (8) and Equation (9) respectively:

$$\begin{aligned}
R^{SH} = & \sin(\lambda)\cos(2\lambda)\cos(2i_h)\sin(\phi) - \cos(\lambda)\cos(\delta)\cos(2i_h)\cos(\phi) \\
& + 0.5\cos(\lambda)\sin(\delta)\sin(2i_h)\sin(2\phi) - 0.5\sin(\lambda)\sin(2\delta)\sin(2i_h)(1 + \sin^2(\phi))
\end{aligned} \tag{9}$$

$$\begin{aligned}
R^{SV} = & \cos(\lambda)\cos(\delta)\cos(i_h)\sin(\phi) - \cos(\lambda)\sin(\delta)\sin(i_h)\cos(2\phi) \\
& + \sin(\lambda)\cos(2\delta)\cos(i_h)\cos(\phi) - 0.5\sin(\lambda)\sin(2\delta)\sin(i_h)\sin(2\phi)
\end{aligned} \tag{10}$$

$$AS_{es} = \sqrt{(R_{SH})^2 + (R_{SV})^2} \tag{11}$$

The horizontal R^{SH} and vertical R^{SV} radiation components were combined into a scalar value using Equation (10).

Radiation-Pattern-Corrected Residuals

Azimuthal variations in the ground-motion can be due to either the radiation pattern or the 3-D velocity structure. The objective of removing the radiation pattern from the residuals is to isolate the path effects due to the 3-D velocity structure from the radiation pattern effects.

Ergodic GMMs from Equation (1) with within-event residuals δW_{es} from Equation (11) were used rather than within-site residual $\delta W S_{es}$ from Partially-Non Ergodic GMMs. The s_0 represents the y-intercept, and the s_1 represents the slope:

$$\delta W_{es} = s_0 + s_1 * \ln(AS_{es} + 0.2) \quad (12)$$

Another important difference between this study and the study by Kotha et al. (2019) was that the logarithm of the radiation pattern was used in Equation (11). The radiation pattern should be a scale factor on the PSA for consistency, indicating the strength of the radiation pattern, since the within-event residual δW_{es} is also in logarithm units. As mentioned earlier, the Y_{es} is the logarithm of the observed ground-motion so the residuals are also the logarithm of the ground-motion and should be added together rather than multiplied by each other. An issue of using the logarithm is that small values of the radiation pattern result in exponentially large negative values. To avoid this complication, 0.2 was added to the radiation pattern AS_{es} .

In Figure 6, the logarithm of the radiation pattern + 0.2 was plotted against δW_{es} for each period. There is statistical evidence that the radiation pattern has a strong effect at larger periods by examining the slope s_1 , which would lay on the x-axis if the radiation pattern had no effect. Table 2 shows the combination of all s_1 and

standard error terms found. The standard error is the uncertainty in the estimates of the coefficients. The standard error has to be low enough to show that the average radiation pattern is physically different from zero. The table also includes t Ratio values, which indicate that the average radiation pattern shows a statistically significant difference from zero at more than a 98% confidence interval if it is bigger than 2. For $T = 0.3$ s to 5 s, the t Ratio was substantially bigger than 2. In Figure 7, the radiation pattern strength, s_1 , is plotted directly against each period to show radiation pattern's period-dependency. The figures show that the radiation pattern is strongest at a period of $T = 1$ s and generally larger at longer periods.

Next, in Figures 8 - 12, for all 14 earthquakes combined, both within-event residuals δW_{es} and radiation-pattern-corrected within-event residuals $\delta W'_{es}$ for all 14 earthquakes are mapped for each period. The areas of darker purple indicate an overprediction of the ground-motion and the areas of yellow show an underprediction of the ground-motion. The plots are shown with and without the location of stations and earthquakes for clarity and reference. The radiation-pattern-corrected within-event residuals $\delta W'_{es}$ are calculated by Equation (12):

$$\delta W'_{es} = \delta W_{es} - s_1 * \ln(AS_{es} + 0.2) \quad (13)$$

For a period of $T = 1$ s (the strongest radiation-pattern-effect), within-event residuals δW_{es} are mapped along with radiation-pattern-corrected within-event residuals $\delta W'_{es}$ for each earthquake (Figures 13 - 26). We can see the comparison between within-event path terms that are clouded by the radiation pattern and the filtered path terms (when the radiation-pattern-effect is removed). The contrast between values are highlighted in

Figures 27 - 40, where the differences between corrected within-event residuals δW_{es} and regular within-event residuals δW_{es} for each earthquake are mapped. Corresponding histograms show the distribution of differences between corrected within-event residuals δW_{es} and regular within-event residuals δW_{es} for each earthquake.

Spatial Autocorrelation Analysis

Since source-to-receiver distances affect wave propagation and attenuation, we analyzed the spatial dependence and distance correlations of within-event residuals δW_{es} in terms of semivariances. In Figure 41, semivariogram plots are shown for $T = 0.2$ s, 0.5 s, 0.75 s, 1 s, 2 s, and 5 s. The period of $T = 0.1$ s has the largest range of 8.73 km, and the period of $T = 10$ s has the smallest range of 2.49 km. This shows the contrast in how the δW_{es} is spatially autocorrelated depending on the period. The corresponding sills are 0.64 and 0.48. If excluding the periods of $T = 7.5$ s and $T = 10$ s since uncertainties are so large, the period of $T = 2$ s has the smallest range of 6.51 km and has a corresponding sill of 0.64. The trend still shows that longer periods have a smaller range. Figure 42 and Table 4 show the complete set of range and sill values.

Implementation into GMMs

Averaged radiation patterns are implicitly included in GMMs through the style-of-faulting since the average of the radiation pattern systematically changes with each type of fault. Since the radiation-pattern-effects show a significant role in moderate Bay Area earthquakes at long periods, explicitly modeling the radiation pattern as part of the source term will increase the accuracy of the source term, and consequently, the

accuracy of the path term due to the 3-D velocity structure. The path effect will no longer be confounded and blurred out by the radiation pattern's impact and will solely be influenced by the 3-D geology. The differences in path terms are distinct when the radiation-pattern-effect is extracted from the δW_{es} . The percentage difference between radiation-pattern-corrected within-event residuals varied by period, with the largest differences at $T = 0.75$ s. Separating the effects of 3-D velocity and radiation pattern will help increase the accuracy of the 3-D velocity structure and give insight into the strength of the radiation-pattern-effect and the 3-D velocity-structure-effect.

Going forward, radiation pattern should be properly categorized. By taking its effect out of the path term, and by modeling it explicitly as part of the source, path effects should be isolated from small earthquakes and then applied to large earthquakes. Though further studies should thoroughly investigate the role of radiation pattern in larger Bay Area earthquakes, it is expected for the radiation-pattern-effect to weaken with increasing magnitude due to the finite rupture dimension (no longer a point source). In between each sub-source there is abundant randomness in the radiation pattern. The exact shape is blurred when the sub sources are combined making the radiation pattern appear more stochastic and less deterministic. The radiation pattern of smaller earthquakes is not fully stochastic because there is solely one sub-source propagating through the 3-D crust (point source).

Ergodic GMMs should have the radiation-pattern-effect removed from the δW_{es} path term in a similar way to this study. Partially Non-Ergodic GMMs should have an anisotropic source and remove the radiation pattern from the $\delta W S_{es}$ path term. In future versions of Fully Non-Ergodic GMMs, the radiation pattern should no longer be part of the unmodeled path term, but rather explicitly modeled as part of the

source in moderate earthquakes. It is important to properly model the radiation pattern as part of the source since aleatory variability will be reduced and lead to a more accurate GMM range to utilize in seismic risk assessments. A combination of both a deterministic-isotropic and stochastic-anisotropic radiation pattern, instead of a perfectly deterministic radiation pattern, is expected to match observed amplitudinal period-dependency. Whether the radiation pattern of an earthquake appears stochastic or deterministic is dependent on the medium's heterogeneity of wave propagation and its corresponding frequency and period. Similar to findings by Takemura et al. (2009) and Kobayashi et al. (2015), strong radiation patterns occurred and had a more substantial impact at highly deterministic longer periods and closer distance to the source as a result of less scattering.

An important distinction should be made, however, that the radiation-pattern-effect for small earthquakes should not be applied to large earthquakes as the radiation-pattern-effects are expected to be reduced for large magnitudes.

Similarly, radiation pattern should also be modeled into physics-based GM simulations, which have the 3-D geology as an explicit input. This will also result in a more accurate, narrow, and usable range of ground-motions. The path effect and source effect will be less confounded and lead to an overall decrease in aleatory variability.

Testing of 3-D velocity structure

Explicitly modeling the radiation pattern and removing it from the path effect provides a check for GM simulations with 3-D geology input. Predictions could be compared against empirical data to see if similar amplitudes will be obtained. Path effects should

be compared using the difference between those left from radiation-pattern-corrected within-event residuals from earthquake data and path effects used in GM simulations with 3-D and 1-D results. The normalization of the 3-D ground-motions by the 1-D ground-motions will remove the average source and distance scaling from the 3-D ground-motions.

GMMs and 1-D simulations differ in accounting for site effects. Site-specific GMM residuals (such as Partially Non-Ergodic and Fully Non-Ergodic models) account for site terms whereas the 1-D simulations use a singular shear-wave velocity profile for the region where site effects are not removed. A systematic difference between the California-averaged V_{S30} scaling GMM and the geology of the Bay Area was found (shown in Figures 43 and 44) where the effect of V_{S30} scaling was analyzed to see its relation with within-event residuals. The V_{S30} scaling was found to have a period-dependence, with larger impacts at larger periods. In Figures 45 - 49, the radiation-pattern-corrected and velocity-corrected within-event residuals are shown against just velocity-corrected within-event residuals (not corrected for radiation pattern). Velocity-corrected within-event residuals are also mapped for comparison. The velocity-correction terms are included in Table 5.

Conclusions

We can see statistically and physically significant evidence that the radiation-pattern-effect is strong — especially at long periods — and needs to be incorporated into GMMs going forward. Current GMMs obscure source and path effects, which unnecessarily add to the aleatory variability. Through explicitly modeling the radiation pattern as

part of the source, a more accurate and narrow range of possible ground motions can be obtained. A complication for utilizing radiation patterns in GMMs is the extrapolation between relating the radiation-pattern-effect for small-magnitude earthquakes to large-magnitudes earthquakes. Larger magnitude earthquakes are expected to have a smaller radiation-pattern-effect, however, 3-D modeling will be needed for addressing the issue.

It is important to compare predicted ground-motions of numerically-based ground-motion simulations and different types of GMMs against observed earthquake ground-motion data to determine if the 3-D velocity structure is leading to more accurate estimates of the ground-motion than simple GMMs with site-specific site terms. The comparison between the path effects seen in the observations from small magnitude earthquakes on the Hayward fault and the radiation-pattern-removed path effects used in 3-D ground-motions show areas for improvement and possibilities for 3-D simulation calibration.

Acknowledgments

This paper was made possible thanks to the funding provided by the Exascale Computing Project at Lawrence Berkeley National Laboratory and the United States Geological Survey.

Permission was obtained to use copyrighted figures from Al Atik et al. (2010) and Kotha et al. (2019).

Figure 1 from Al Atik et al. (2010) was used under the SSA Permissions Policy which permits: use of up to three figures/tables/images from a journal article, but not more than six figures/tables/images from an annual journal volume for republication in a

journal or book chapter, use of text extracts of less than 400 words from a journal article, but not more than a total of 800 words from a journal issue, and use of a maximum of 30 figures/tables/images from the Seismological Society of America's journals in any given book, no matter how many authors, chapter contributors or volumes it has.

Figures 2 - 4 from Kotha et al. (2019) are licensed under a Creative Commons Attribution 4.0 International License which permits use, sharing, adaptation, distribution and reproduction in any medium or format, as long as appropriate credit to the original author(s) and the source given, a link to the Creative Commons license is provided, and if changes were made they are indicated.

No changes were made to all images and the Creative Commons license is as follows:

<http://creativecommons.org/licenses/by/4.0/>

References

- Abrahamson, N. A. (2008). Ground Motion Models. *Geotechnical Earthquake Engineering and Soil Dynamics IV 181*, 1-31. doi: [https://doi.org/10.1061/40975\(318\)2](https://doi.org/10.1061/40975(318)2)
- Abrahamson, N. A., Silva, W. J., Kamai, R. (2014). Summary of the ASK14 Ground Motion Relation for Active Crustal Regions. *Earthquake Spectra 30(3)*, 1025–1055. doi: <https://doi.org/10.1193/070913EQS198M>
- Al Atik, L., Abrahamson, N. A., Bommer, J. J., Scherbaum, F., Cotton, F., Kuehn, N. (2010). The Variability of Ground-Motion Prediction Models and Its Components. *Seismological Research Letters 81(5)*, 794–801. doi: <https://doi.org/10.1785/gssrl.81.5.794>
- Ancheta, T. D., Darragh, R. B., Stewart, J. P., Seyhan, E., Silva, W. J., Chiou, B. S., Wooddell, K. E., Graves, R. W., Kottke, A. R., Boore, D. M., Kishida, T., Donahue, J. L. (2014). NGA-West2 Database. *Earthquake Spectra 30(3)*, 989–1005. doi: <https://doi.org/10.1193/070913EQS197M>
- Boore, D. M., Watson-Lamprey, J., Abrahamson, N. A. (2006). Orientation-Independent Measures of Ground-Motion. *Bulletin of the Seismological Society of America 96(4A)*, 1502–1511. doi: <https://doi.org/10.1785/0120050209>
- Brocher T., Aagaard B., Simpson R., Jachens R. (2006). The new USGS 3D seismic velocity model for Northern California (abstract). *Seismological Research Letters 77(2)*.
- Crotwell, H. P., Owens, T. J., Ritsema J. (1999). The TauP Toolkit: Flexible seismic travel-time and ray-path utilities. *Seismological Research Letters 70*, 154–160.

- Dawood, H. M., Rodriguez-Marek, A., Bayless, J., Goulet, C., Thompson, E. (2016). A Flatfile for the KiK-net Database Processed Using an Automated Protocol. *Earthquake Spectra* 32(3), 1281–1302. doi: <https://doi.org/10.1193/071214eqs106>
- Kobayashi, M., Takemura, S., Yoshimoto, K. (2015). Frequency and distance changes in the apparent P-wave radiation pattern: effects of seismic wave scattering in the crust inferred from dense seismic observations and numerical simulations. *Geophysical Journal International* 202(3), 1895–1907. doi: <https://doi.org/10.1093/gji/ggv263>
- Kotha, S. R., Cotton, F., Bindi, D. (2010). Empirical Models of Shear-Wave Radiation Pattern Derived from Large Datasets of Ground-Shaking Observations. *Scientific Reports* 9. doi: <https://doi.org/10.1038/s41598-018-37524-4>
- Sirovich, L. (1994). A case of the influence of radiation pattern on peak accelerations. *Bulletin of the Seismological Society of America* 84(5), 1658–1664. doi: <https://doi.org/10.1785/BSSA0840051658>
- Takemura, S., Furumura, T., Saito, T. (2009). Distortion of the apparent S-wave radiation pattern in the high-frequency wavefield: Tottori-Ken Seibu, Japan, earthquake of 2000. *Geophysical Journal International* 178(2), 950–961. doi: <https://doi.org/10.1111/j.1365-246X.2009.04210.x>

Full Mailing Address for Each Author

Irene Liou

2001 Ghuasi Hall

Department of Civil & Environmental Engineering

University of California

Davis, CA 95616

Norman Abrahamson

455 Davis Hall

Department of Civil & Environmental Engineering

University of California

Berkeley, CA 94720

List of Figures

1	Example of between-event δB and within-event δW residuals in ground-motion variability of two sample earthquakes (Al Atik et al. 2010).	25
2	Strikeslip events from Japan and Global data sets show $\delta W S$ (in black) and averaged $\delta W S$ (in red) displayed against theoretical S-wave radiation patterns (blue) for $T = 0.1$ s, 0.5 s, and 1 s (Kotha et al. 2019).	26
3	Normal-, Oblique-, and Reverse-faulting events from Japan data sets show $\delta W S$ (black) and averaged $\delta W S$ (in red) displayed against theoretical S-wave radiation patterns (blue) for $T = 0.1$ s, 0.5 s, and 1 s (Kotha et al. 2019).	27
4	Period-, distance- and style-of-faulting dependent anisotropic ground-shaking amplification predictions for four events in Japan (NM: Normal, OB: Oblique, RS: Reverse, and SS: Strike-slip) in respect to median-isotropic predictions. The systematic higher (red) and lower (blue) differences are displayed for $T = 0.1$ s, 0.5 s, and 1 s (Kotha et al. 2019).	28
5	Fourteen moderate magnitude (M3.0-4.9) Bay Area earthquakes.	29
6	Within-event residual δW_{es} dependence on radiation pattern $AS_{es} + 0.2$ at $T = 0.2$ s, 0.5 s, 0.75 s, 1 s, 2 s, and 5 s in logarithm units.	30
7	Radiation-pattern-effect S_1 dependence on period T (s).	31
8	δW_{es} and radiation-pattern-corrected δW_{es} for all earthquakes at $T = 0.2$ s.	32
9	δW_{es} and radiation-pattern-corrected δW_{es} for all earthquakes at $T = 0.5$ s.	33
10	δW_{es} and radiation-pattern-corrected δW_{es} for all earthquakes at $T = 1$ s.	34

11	δW_{es} and radiation-pattern-corrected δW_{es} for all earthquakes at $T = 2$ s.	35
12	δW_{es} and radiation-pattern-corrected δW_{es} for all earthquakes at $T = 5$ s.	36
13	δW_{es} and radiation-pattern-corrected δW_{es} for the M3.5 May 14th, 2018 Oakland earthquake at $T = 1$ s.	37
14	δW_{es} and radiation-pattern-corrected δW_{es} for the M3.6 October 27th, 2011 Berkeley earthquake at $T = 1$ s.	37
15	δW_{es} and radiation-pattern-corrected δW_{es} for the M3.8 October 20th, 2011 Berkeley earthquake at $T = 1$ s.	38
16	δW_{es} and radiation-pattern-corrected δW_{es} for the M4.0 October 20th, 2011 Berkeley earthquake at $T = 1$ s.	38
17	δW_{es} and radiation-pattern-corrected δW_{es} for the M4.0 March 5th, 2012 El Cerrito earthquake at $T = 1$ s.	39
18	δW_{es} and radiation-pattern-corrected δW_{es} for the M4.4 January 4th, 2018 Berkeley earthquake at $T = 1$ s.	39
19	δW_{es} and radiation-pattern-corrected δW_{es} for the M4.0 August 17th, 2015 Piedmont earthquake at $T = 1$ s.	40
20	δW_{es} and radiation-pattern-corrected δW_{es} for the M4.9 May 13th, 2002 Gilroy earthquake at $T = 1$ s.	40
21	δW_{es} and radiation-pattern-corrected δW_{es} for the M3.5 October 5th, 2019 Colma earthquake at $T = 1$ s.	41
22	δW_{es} and radiation-pattern-corrected δW_{es} for the M4.0 July 21st, 2015 Fremont earthquake at $T = 1$ s.	41
23	δW_{es} and radiation-pattern-corrected δW_{es} for the M4.5 October 14th, 2019 Pleasant Hill earthquake at $T = 1$ s.	42

24	δW_{es} and radiation-pattern-corrected δW_{es} for the M3.5 November 10th, 2018 Crockett earthquake at $T = 1$ s.	42
25	δW_{es} and radiation-pattern-corrected δW_{es} for the M3.9 December 26th, 2017 Alum Rock earthquake at $T = 1$ s.	43
26	δW_{es} and radiation-pattern-corrected δW_{es} for the M4.3 July 16th, 2019 Byron earthquake at $T = 1$ s.	43
27	The mapped distribution and histogram distribution of differences be- tween δW_{es} and radiation-pattern-corrected δW_{es} for the M3.5 May 14th, 2018 Oakland earthquake at $T = 1$ s.	44
28	The mapped distribution and histogram distribution of differences be- tween δW_{es} and radiation-pattern-corrected δW_{es} for the M3.6 October 27th, 2011 Berkeley earthquake at $T = 1$ s.	44
29	The mapped distribution and histogram distribution of differences be- tween δW_{es} and radiation-pattern-corrected δW_{es} for the M3.8 October 20th, 2011 Berkeley earthquake at $T = 1$ s.	45
30	The mapped distribution and histogram distribution of differences be- tween δW_{es} and radiation-pattern-corrected δW_{es} for the M4.0 October 20th, 2011 Berkeley earthquake at $T = 1$ s.	45
31	The mapped distribution and histogram distribution of differences be- tween δW_{es} and radiation-pattern-corrected δW_{es} for the M4.0 March 5th, 2012 El Cerrito earthquake at $T = 1$ s.	46
32	The mapped distribution and histogram distribution of differences be- tween δW_{es} and radiation-pattern-corrected δW_{es} for the M4.4 January 4th, 2018 Berkeley earthquake at $T = 1$ s.	46

33	The mapped distribution and histogram distribution of differences between δW_{es} and radiation-pattern-corrected δW_{es} for the M4.0 August 17th, 2015 Piedmont earthquake at $T = 1$ s.	47
34	The mapped distribution and histogram distribution of differences between δW_{es} and radiation-pattern-corrected δW_{es} for the M4.9 May 13th, 2002 Gilroy earthquake at $T = 1$ s.	47
35	The mapped distribution and histogram distribution of differences between δW_{es} and radiation-pattern-corrected δW_{es} for the M3.5 October 5th, 2019 Colma earthquake at $T = 1$ s.	48
36	The mapped distribution and histogram distribution of differences between δW_{es} and radiation-pattern-corrected δW_{es} for the M4.0 July 21st, 2015 Fremont earthquake at $T = 1$ s.	48
37	The mapped distribution and histogram distribution of differences between δW_{es} and radiation-pattern-corrected δW_{es} for the M4.5 October 14th, 2019 Pleasant Hill earthquake at $T = 1$ s.	49
38	The mapped distribution and histogram distribution of differences between δW_{es} and radiation-pattern-corrected δW_{es} for the M3.5 November 10th, 2018 Crockett earthquake at $T = 1$ s.	49
39	The mapped distribution and histogram distribution of differences between δW_{es} and radiation-pattern-corrected δW_{es} for the M3.9 December 26th, 2017 Alum Rock earthquake at $T = 1$ s.	50
40	The mapped distribution and histogram distribution of differences between δW_{es} and radiation-pattern-corrected δW_{es} for the M4.3 July 16th, 2019 Byron earthquake at $T = 1$ s.	50

41	Semivariogram of within-event residuals δW_{es} at $T = 0.2$ s, 0.5 s, 0.75 s, 1 s, 2 s, and 5 s.	51
42	Semivariogram values by period T (s).	52
43	V_{S30} dependence of within-event residuals δW_{es} at $T = 0.2$ s, 0.5 s, 0.75 s, 1 s, 2 s, and 5 s in logarithm units.	53
44	δW_{es} and radiation-pattern-corrected δW_{es} for the M3.6 October 27th, 2011 Berkeley earthquake at $T = 1$ s.	54
45	Velocity-corrected δW_{es} and both velocity-corrected and radiation-pattern- corrected δW_{es} for all earthquakes at $T = 0.2$ s.	55
46	Velocity-corrected δW_{es} and both velocity-corrected and radiation-pattern- corrected δW_{es} for all earthquakes at $T = 0.5$ s.	56
47	Velocity-corrected δW_{es} and both velocity-corrected and radiation-pattern- corrected δW_{es} for all earthquakes at $T = 1$ s.	57
48	Velocity-corrected δW_{es} and both velocity-corrected and radiation-pattern- corrected δW_{es} for all earthquakes at $T = 2$ s.	58
49	Velocity-corrected δW_{es} and both velocity-corrected and radiation-pattern- corrected δW_{es} for all earthquakes at $T = 5$ s.	59

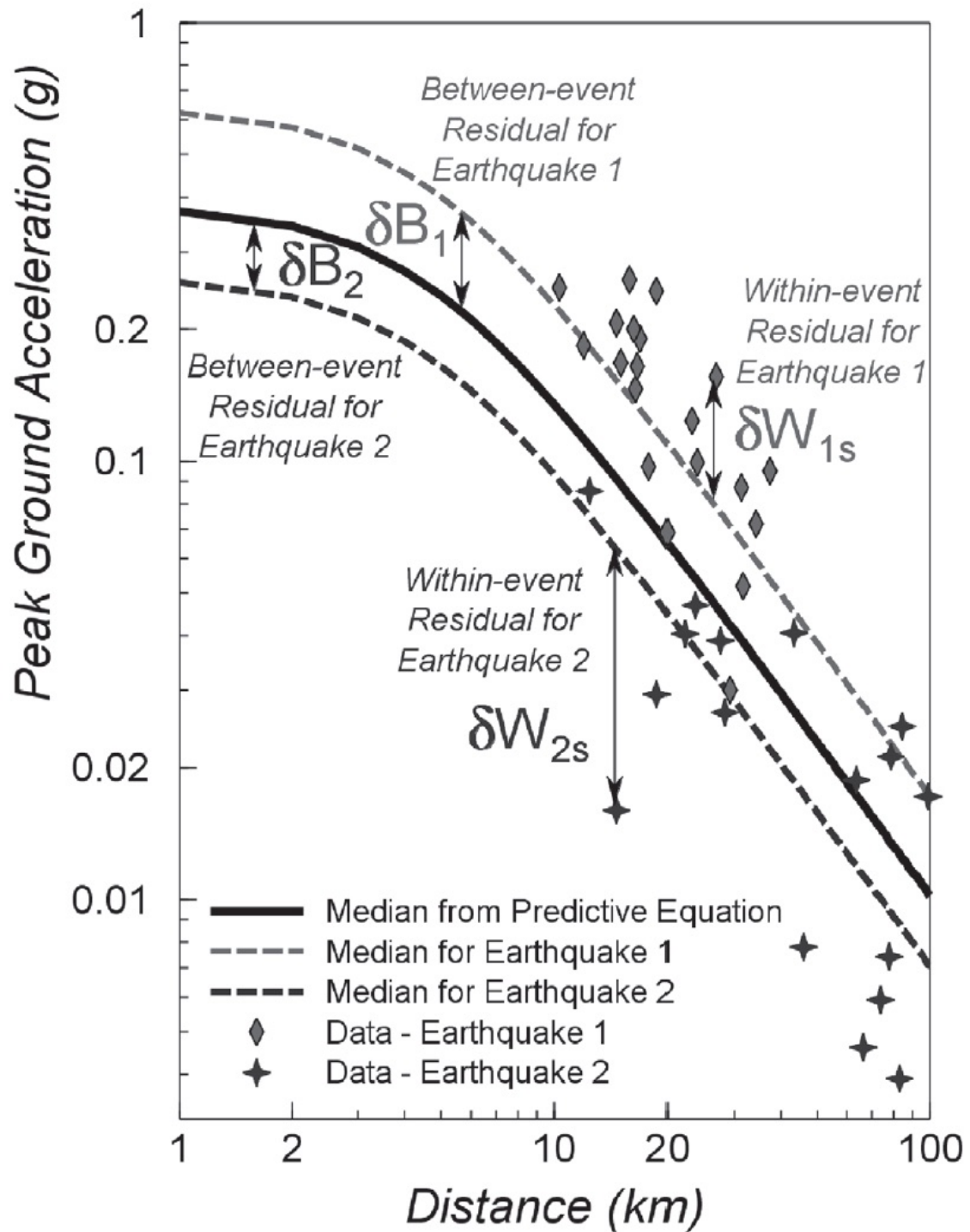


Figure 1: Example of between-event δB and within-event δW residuals in ground-motion variability of two sample earthquakes (Al Atik et al. 2010).

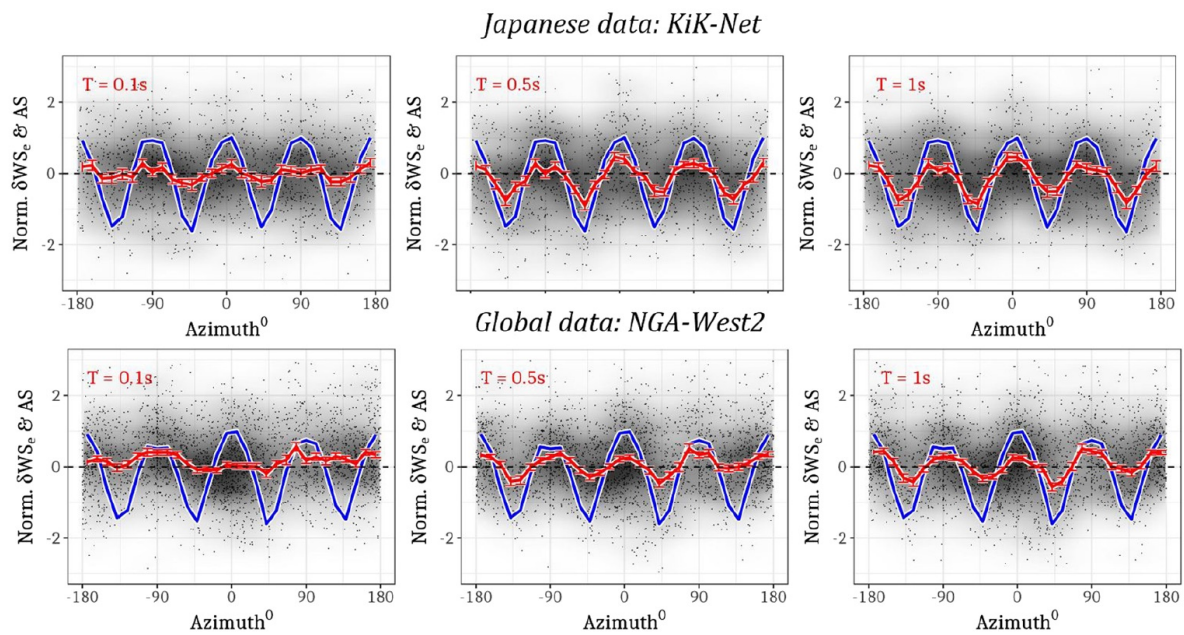


Figure 2: Strikeslip events from Japan and Global data sets show δWS (in black) and averaged δWS (in red) displayed against theoretical S-wave radiation patterns (blue) for $T = 0.1$ s, 0.5 s, and 1 s (Kotha et al. 2019).

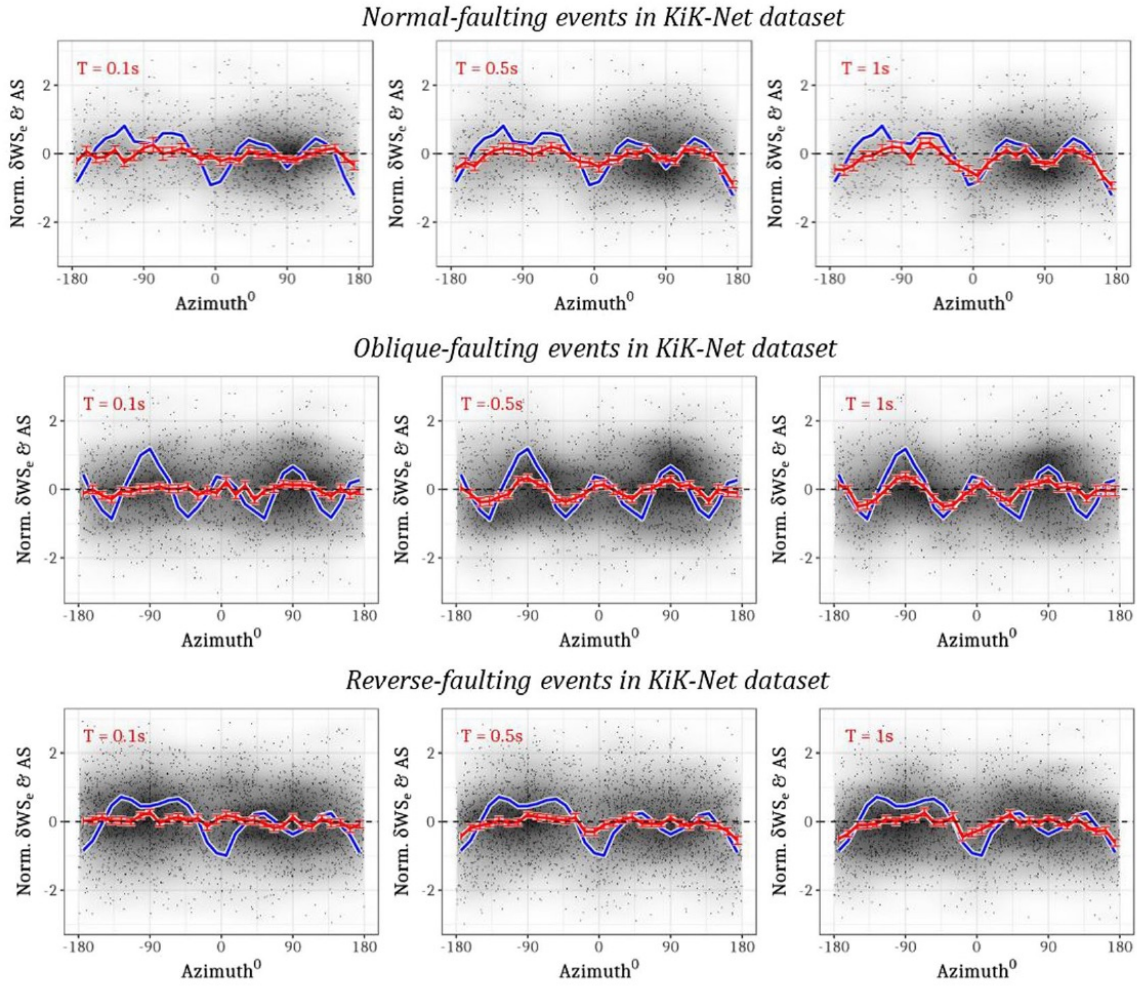


Figure 3: Normal-, Oblique-, and Reverse-faulting events from Japan data sets show δWS (black) and averaged δWS (in red) displayed against theoretical S-wave radiation patterns (blue) for $T = 0.1$ s, 0.5 s, and 1 s (Kotha et al. 2019).

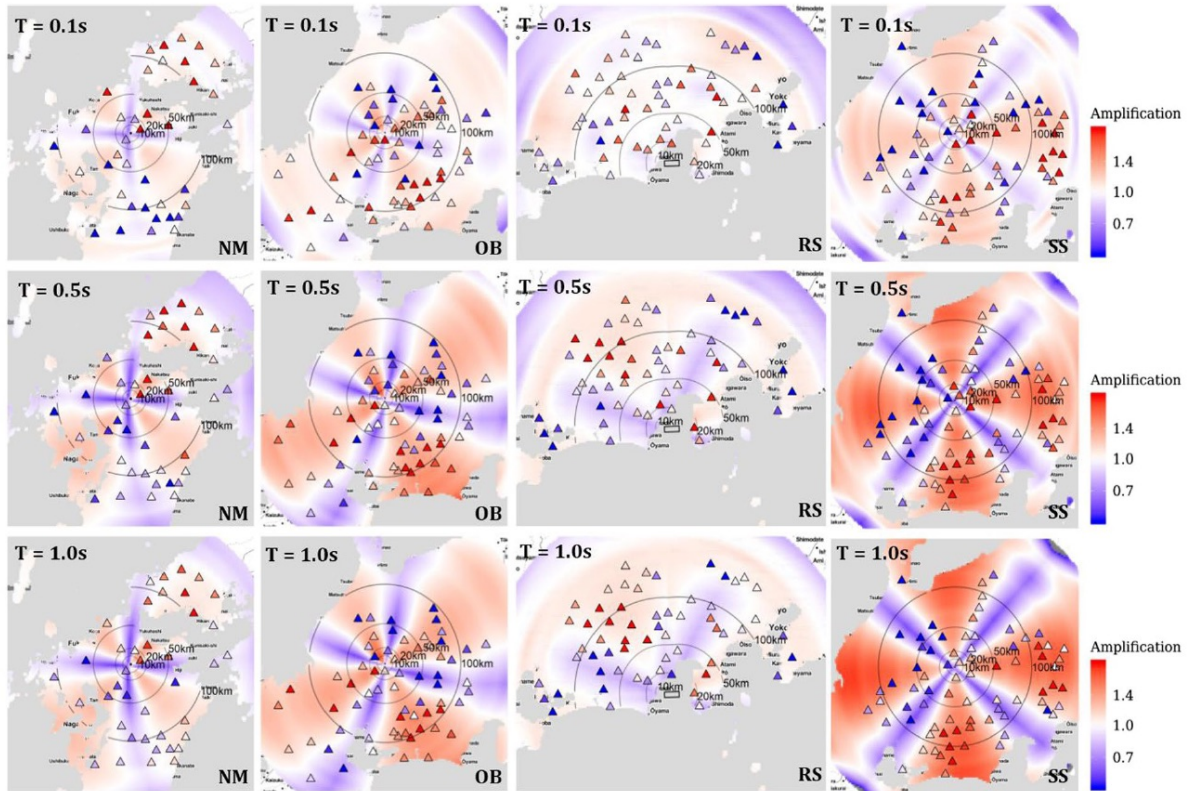


Figure 4: Period-, distance- and style-of-faulting dependent anisotropic ground-shaking amplification predictions for four events in Japan (NM: Normal, OB: Oblique, RS: Reverse, and SS: Strike-slip) in respect to median-isotropic predictions. The systematic higher (red) and lower (blue) differences are displayed for $T = 0.1$ s, 0.5 s, and 1 s (Kotha et al. 2019).

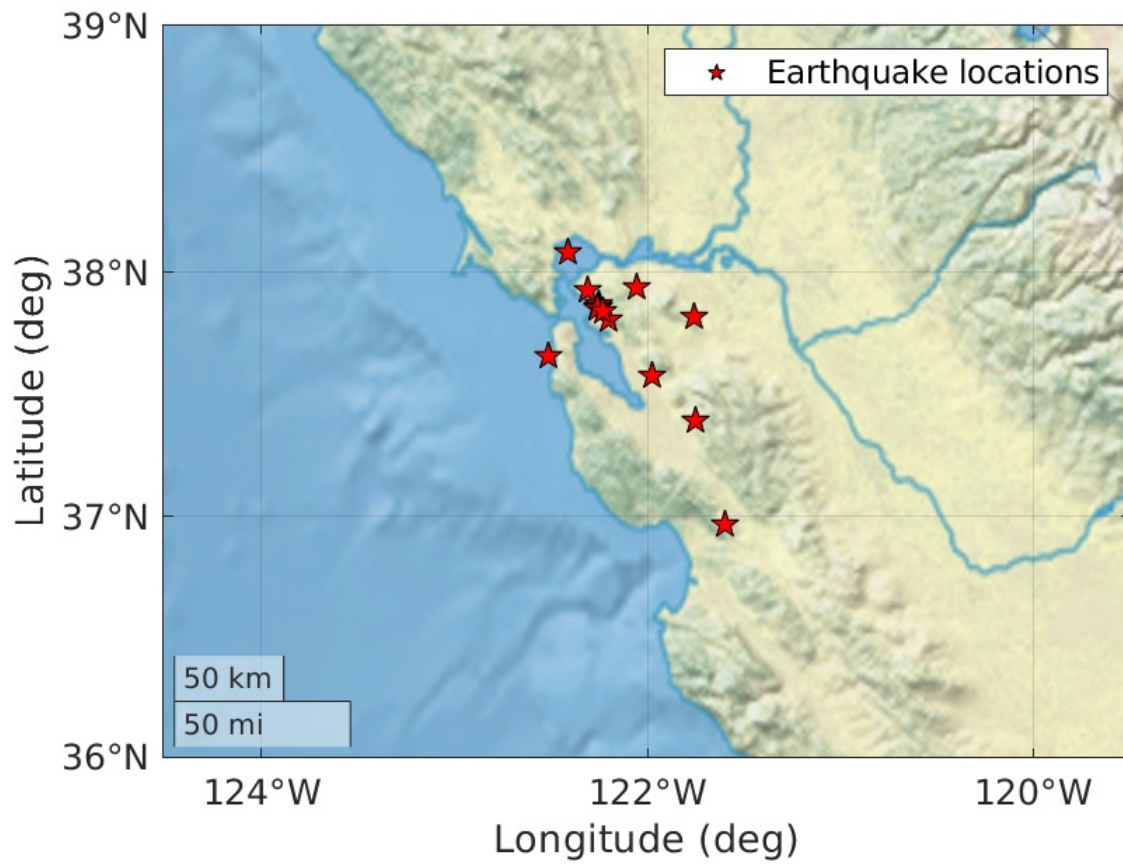
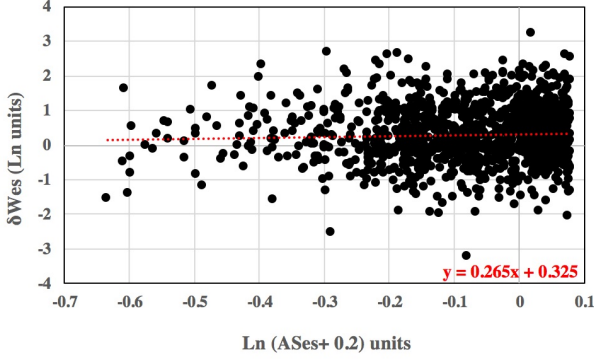
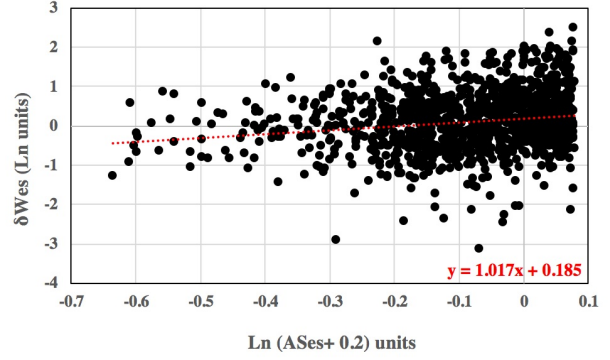


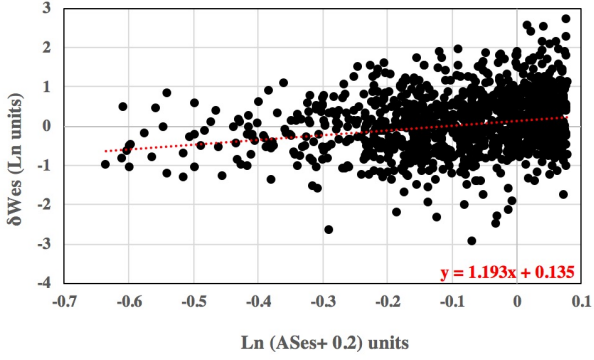
Figure 5: Fourteen moderate magnitude (M3.0-4.9) Bay Area earthquakes.



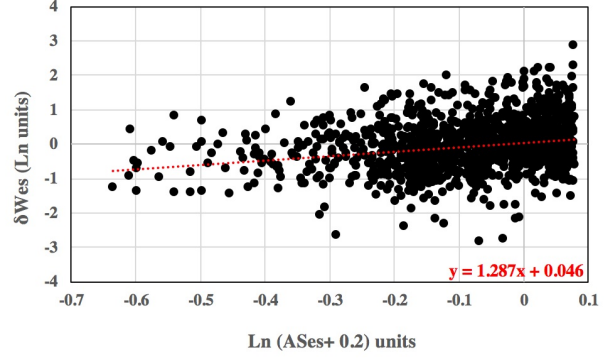
(a) $T = 0.2$ s



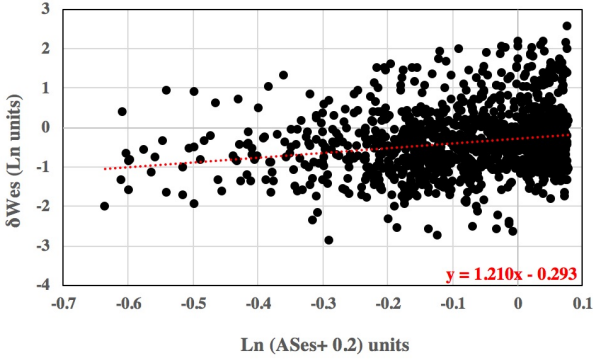
(b) $T = 0.5$ s



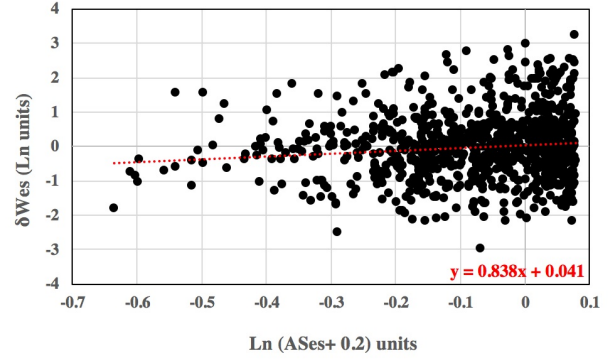
(c) $T = 0.75$ s



(d) $T = 1$ s



(e) $T = 2$ s



(f) $T = 5$ s

Figure 6: Within-event residual δW_{es} dependence on radiation pattern $AS_{es} + 0.2$ at $T = 0.2$ s, 0.5 s, 0.75 s, 1 s, 2 s, and 5 s in logarithm units.

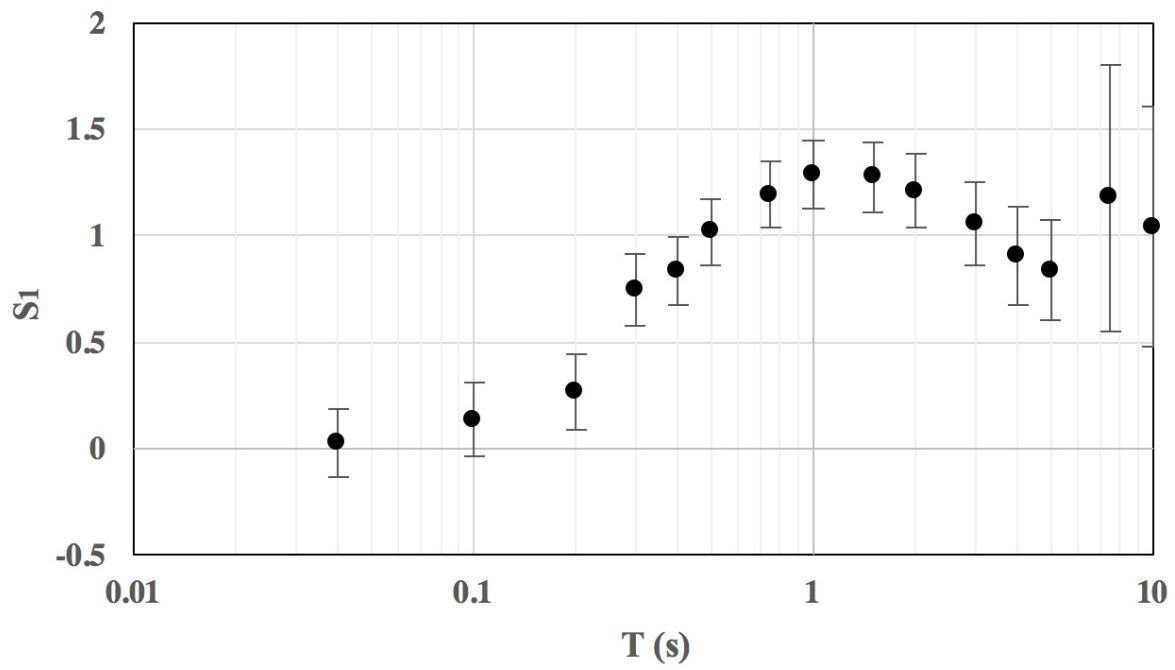
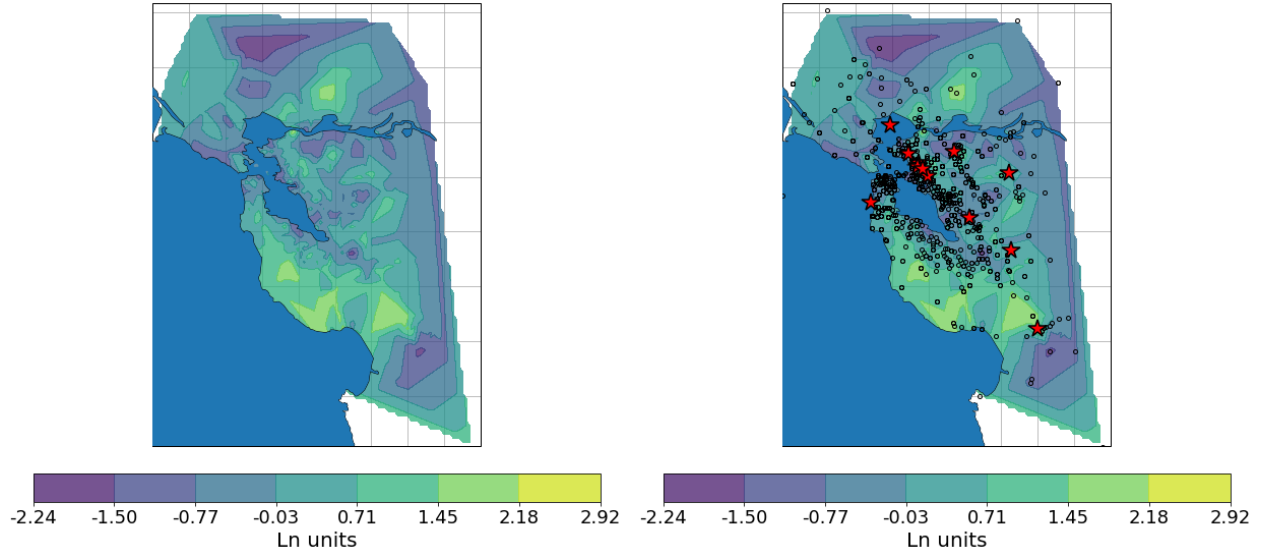
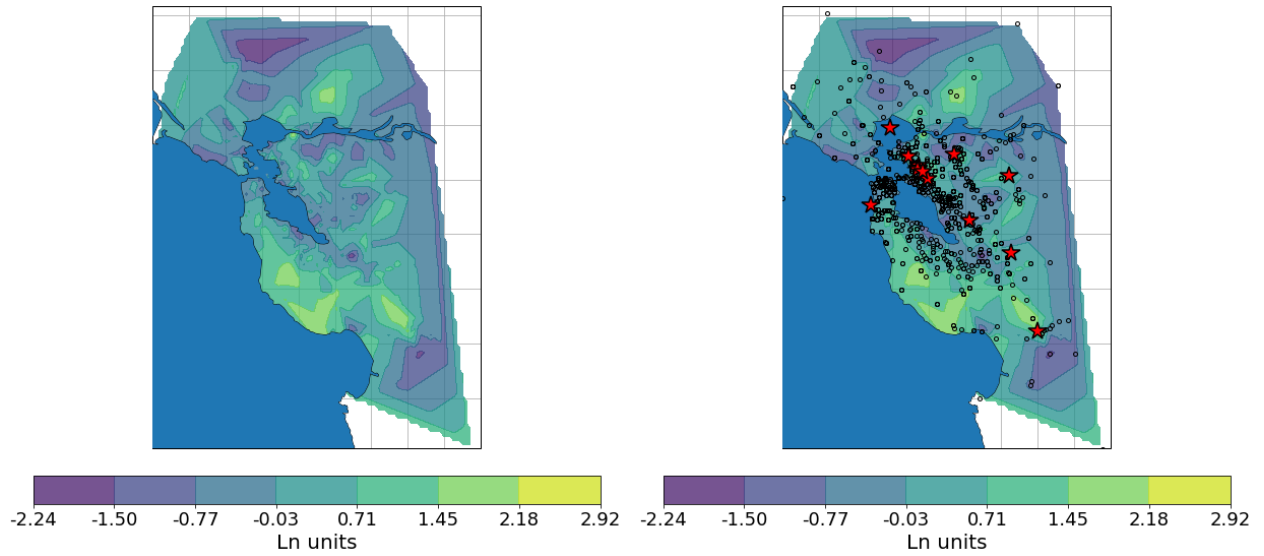


Figure 7: Radiation-pattern-effect S_1 dependence on period T (s).



(a) Within-event residuals δW_{es}

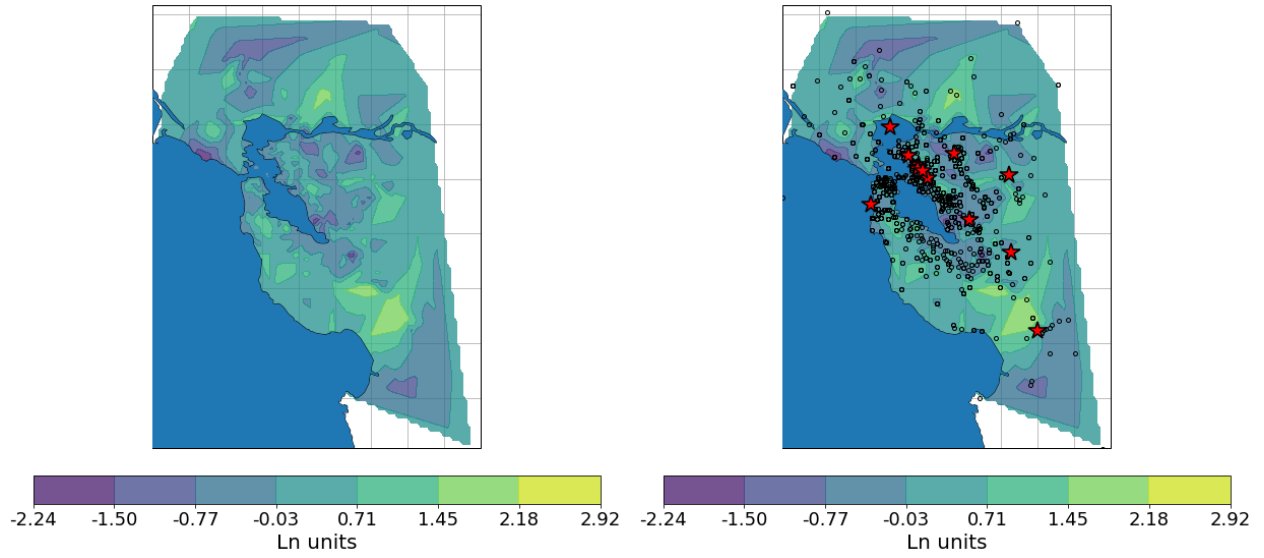
(b) Within-event residuals δW_{es}



(c) Radiation-pattern-corrected δW_{es}

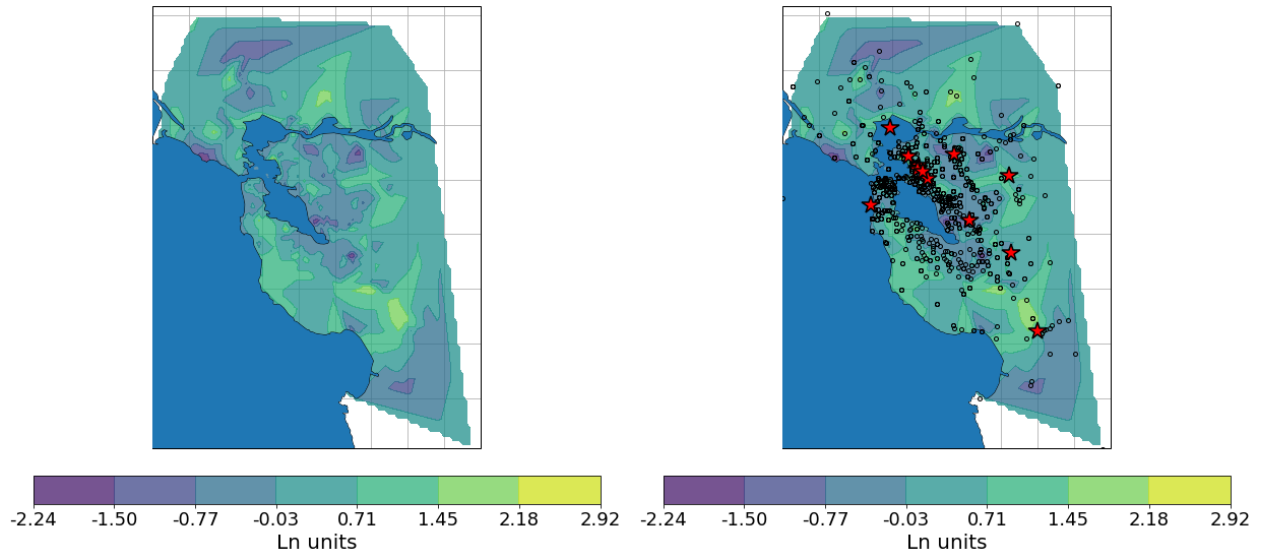
(d) Radiation-pattern-corrected δW_{es}

Figure 8: δW_{es} and radiation-pattern-corrected δW_{es} for all earthquakes at $T = 0.2$ s.



(a) Within-event residuals δW_{es}

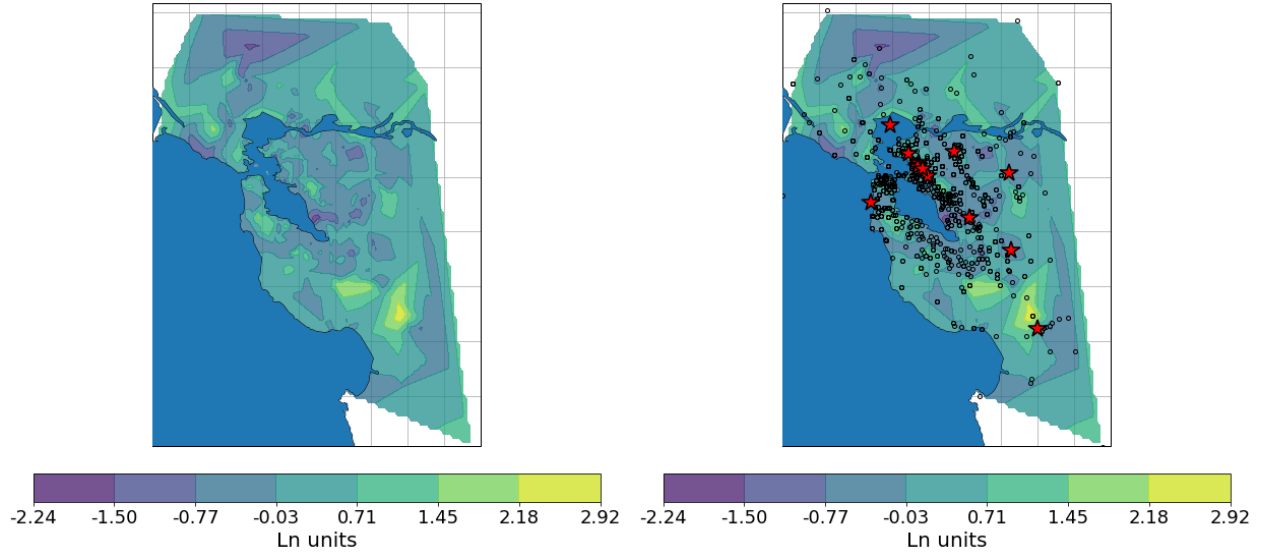
(b) Within-event residuals δW_{es}



(c) Radiation-pattern-corrected δW_{es}

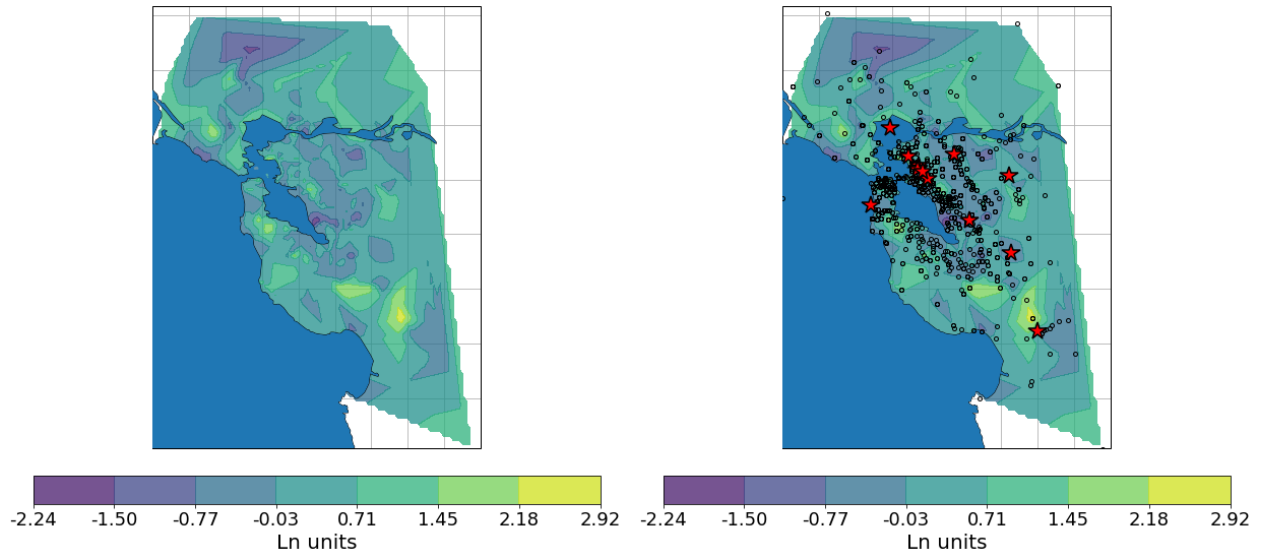
(d) Radiation-pattern-corrected δW_{es}

Figure 9: δW_{es} and radiation-pattern-corrected δW_{es} for all earthquakes at $T = 0.5$ s.



(a) Within-event residuals δW_{es}

(b) Within-event residuals δW_{es}



(c) Radiation-pattern-corrected δW_{es}

(d) Radiation-pattern-corrected δW_{es}

Figure 10: δW_{es} and radiation-pattern-corrected δW_{es} for all earthquakes at $T = 1$ s.

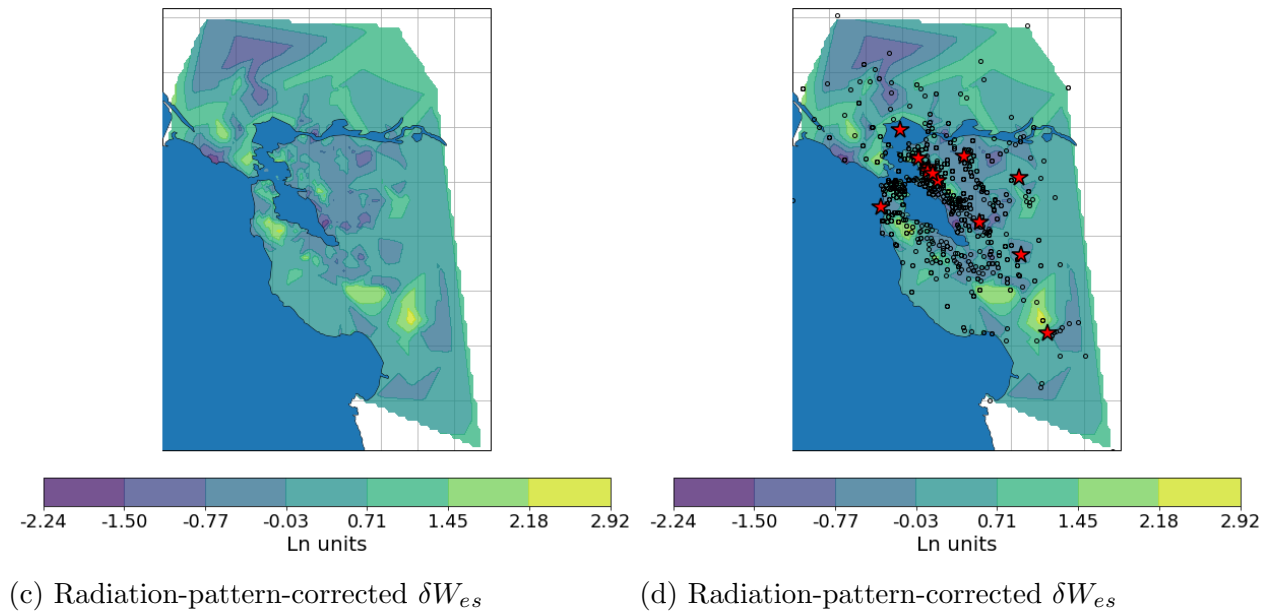
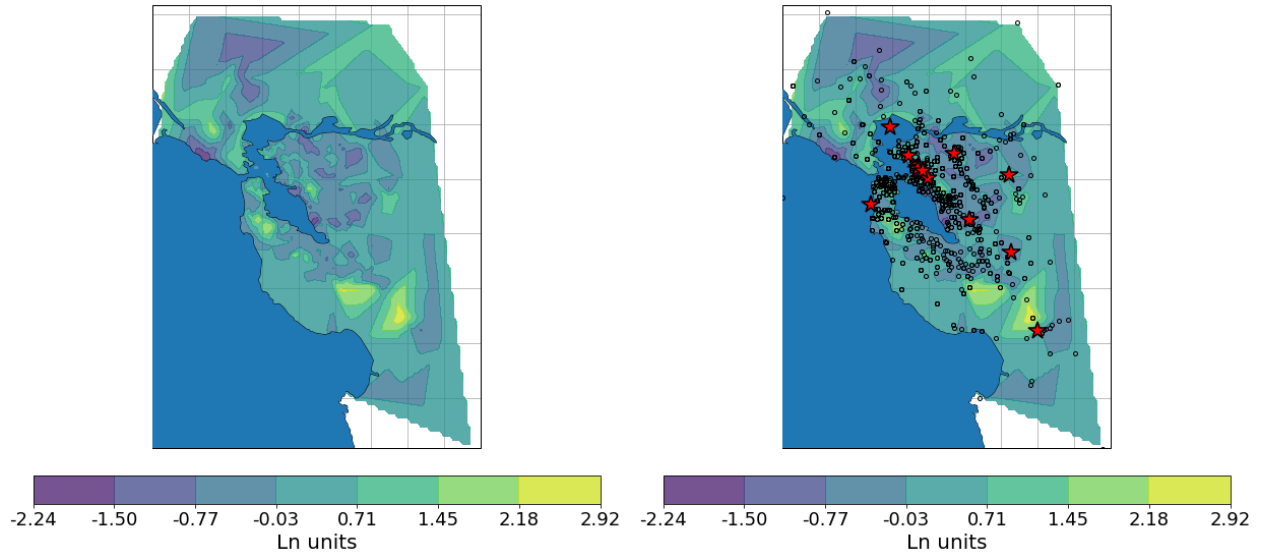
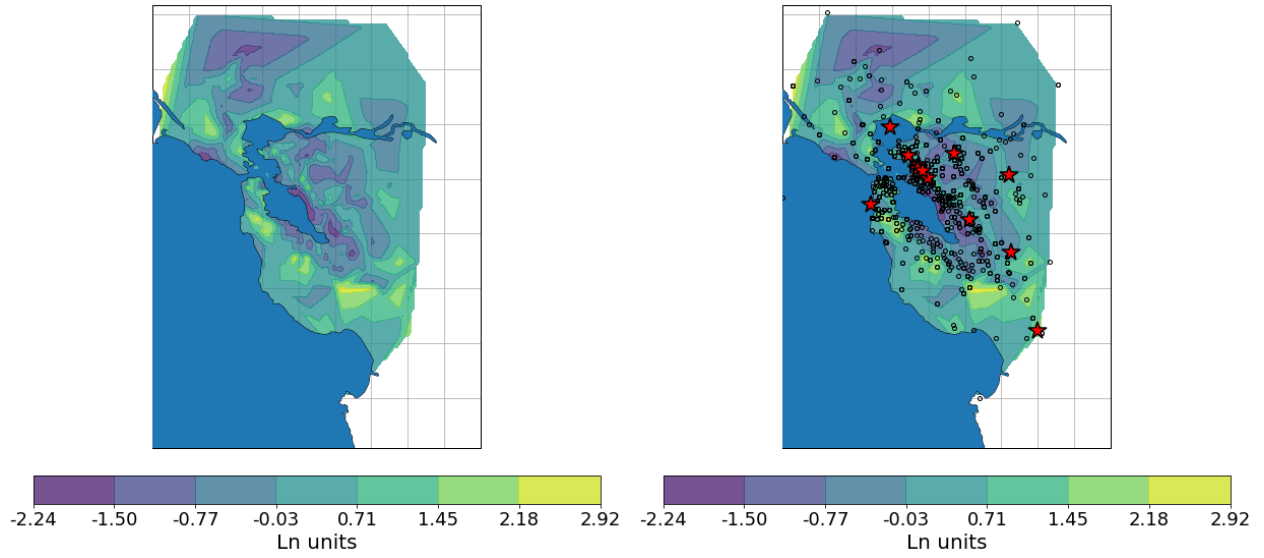
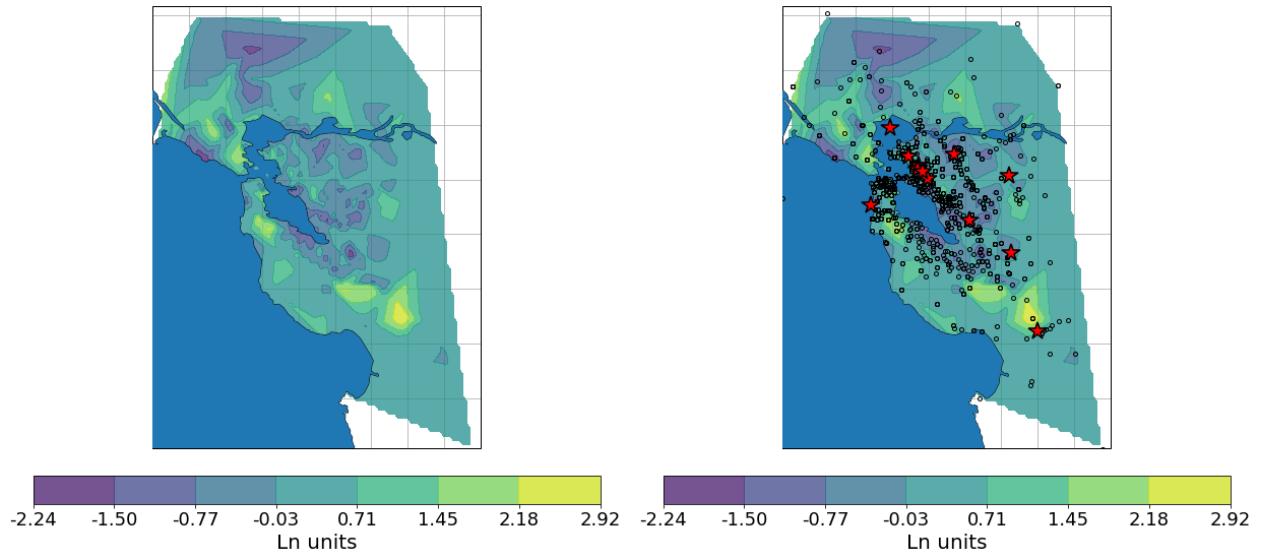


Figure 11: δW_{es} and radiation-pattern-corrected δW_{es} for all earthquakes at $T = 2$ s.



(a) Within-event residuals δW_{es}

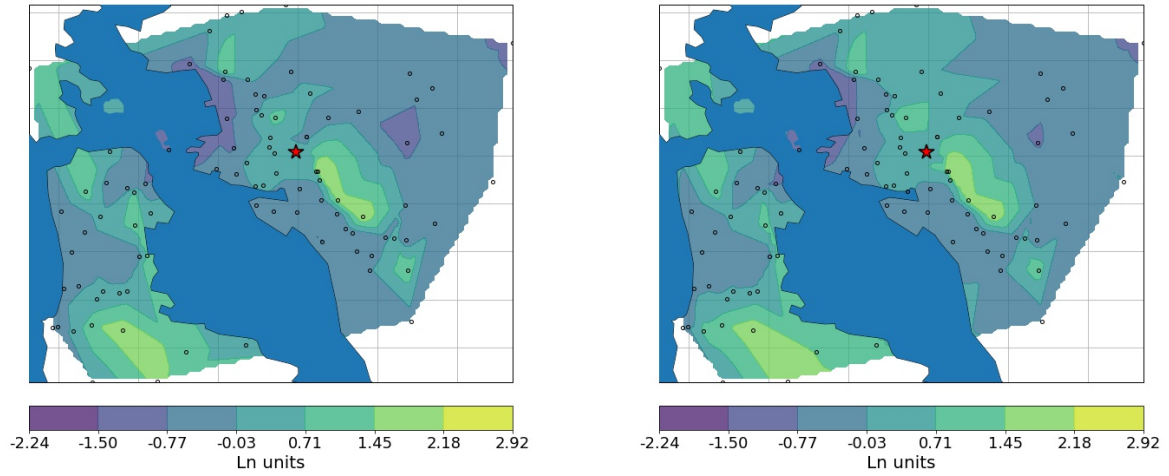
(b) Within-event residuals δW_{es}



(c) Radiation-pattern-corrected δW_{es}

(d) Radiation-pattern-corrected δW_{es}

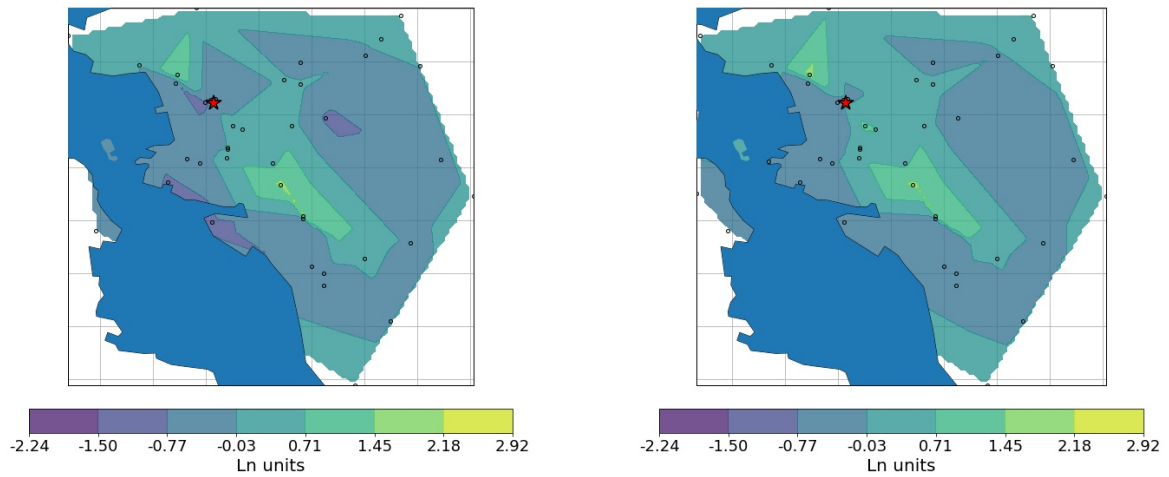
Figure 12: δW_{es} and radiation-pattern-corrected δW_{es} for all earthquakes at $T = 5$ s.



(a) Within-event residuals δW_{es}

(b) Radiation-pattern-corrected δW_{es}

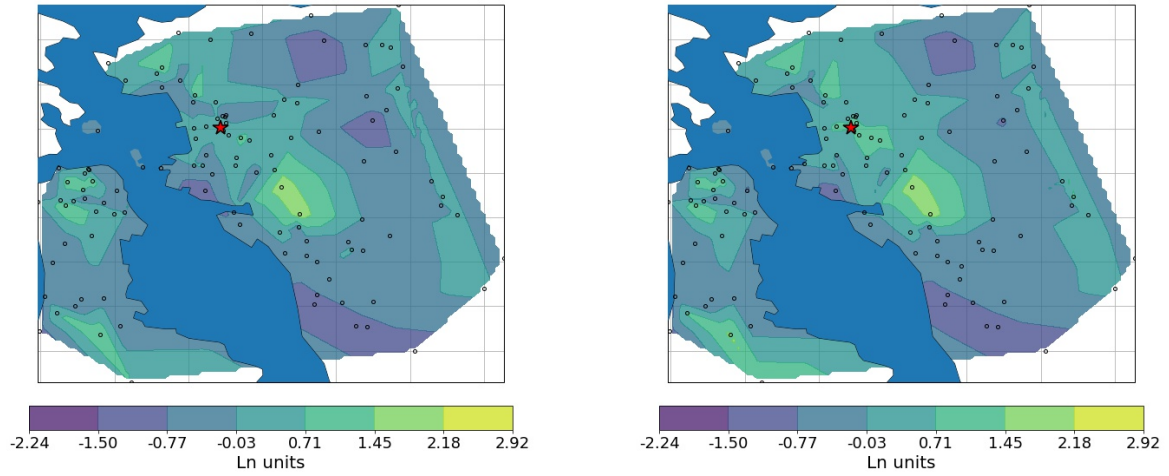
Figure 13: δW_{es} and radiation-pattern-corrected δW_{es} for the M3.5 May 14th, 2018 Oakland earthquake at $T = 1$ s.



(a) Within-event residuals δW_{es}

(b) Radiation-pattern-corrected δW_{es}

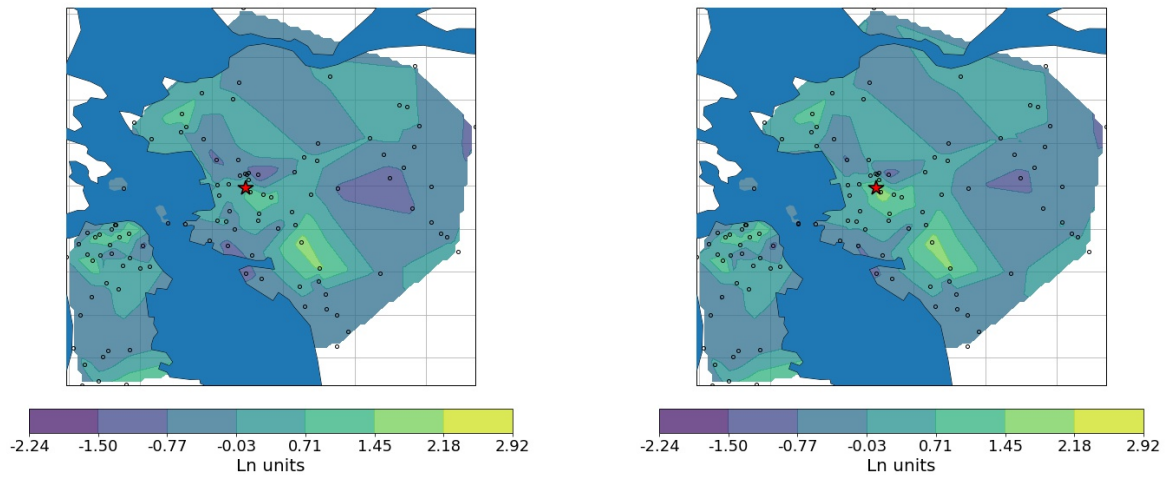
Figure 14: δW_{es} and radiation-pattern-corrected δW_{es} for the M3.6 October 27th, 2011 Berkeley earthquake at $T = 1$ s.



(a) Within-event residuals δW_{es}

(b) Radiation-pattern-corrected δW_{es}

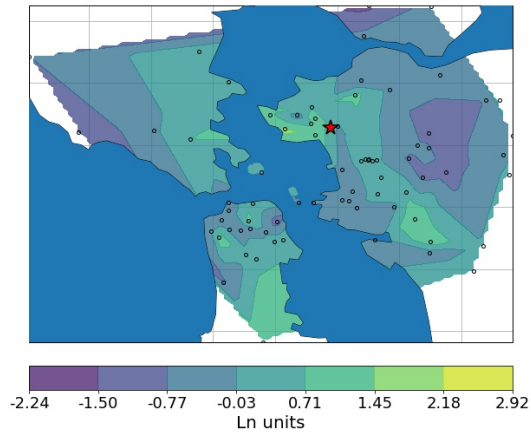
Figure 15: δW_{es} and radiation-pattern-corrected δW_{es} for the M3.8 October 20th, 2011 Berkeley earthquake at $T = 1$ s.



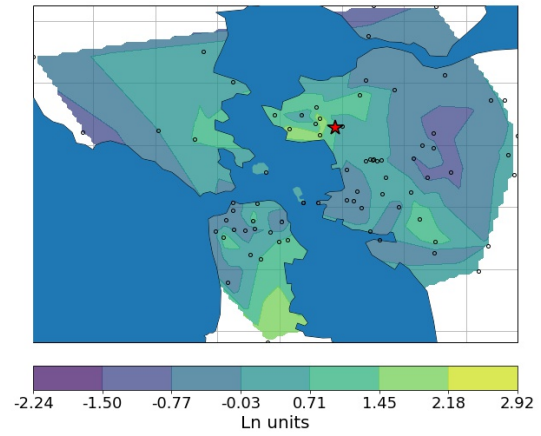
(a) Within-event residuals δW_{es}

(b) Radiation-pattern-corrected δW_{es}

Figure 16: δW_{es} and radiation-pattern-corrected δW_{es} for the M4.0 October 20th, 2011 Berkeley earthquake at $T = 1$ s.

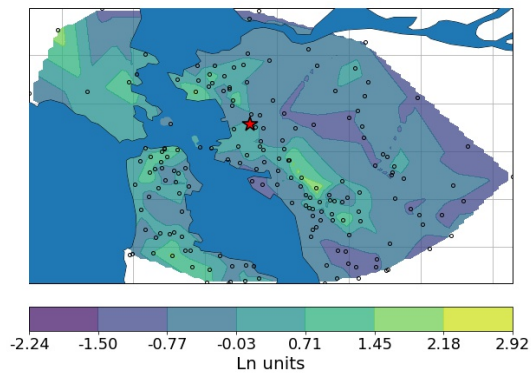


(a) Within-event residuals δW_{es}

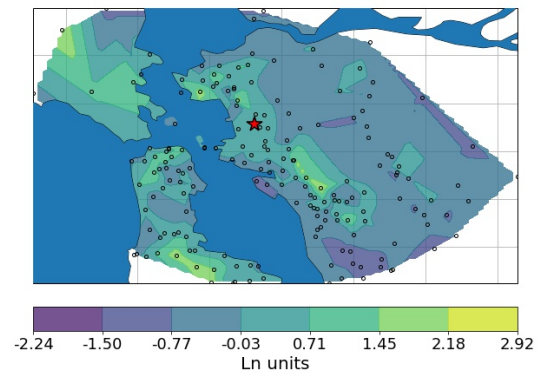


(b) Radiation-pattern-corrected δW_{es}

Figure 17: δW_{es} and radiation-pattern-corrected δW_{es} for the M4.0 March 5th, 2012 El Cerrito earthquake at $T = 1$ s.

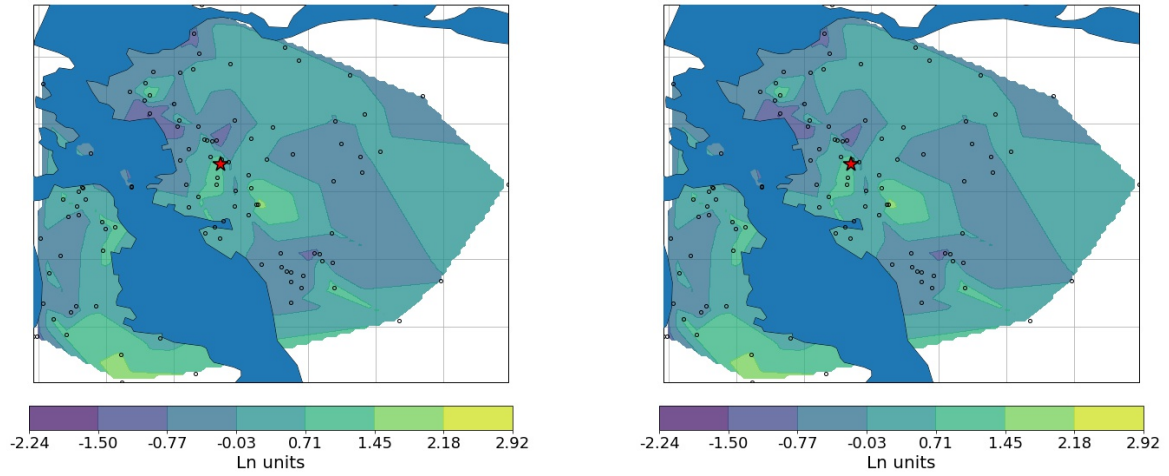


(a) Within-event residuals δW_{es}



(b) Radiation-pattern-corrected δW_{es}

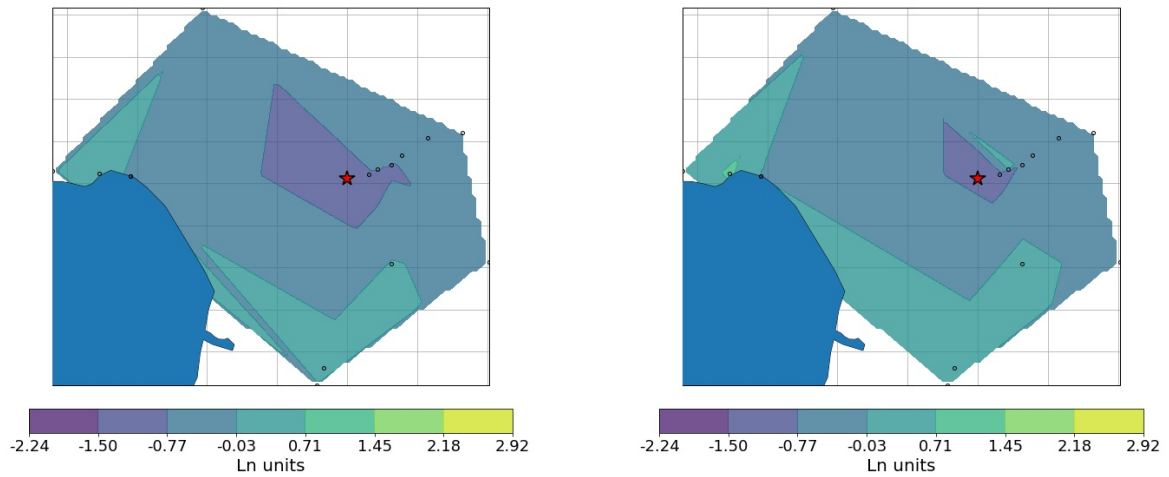
Figure 18: δW_{es} and radiation-pattern-corrected δW_{es} for the M4.4 January 4th, 2018 Berkeley earthquake at $T = 1$ s.



(a) Within-event residuals δW_{es}

(b) Radiation-pattern-corrected δW_{es}

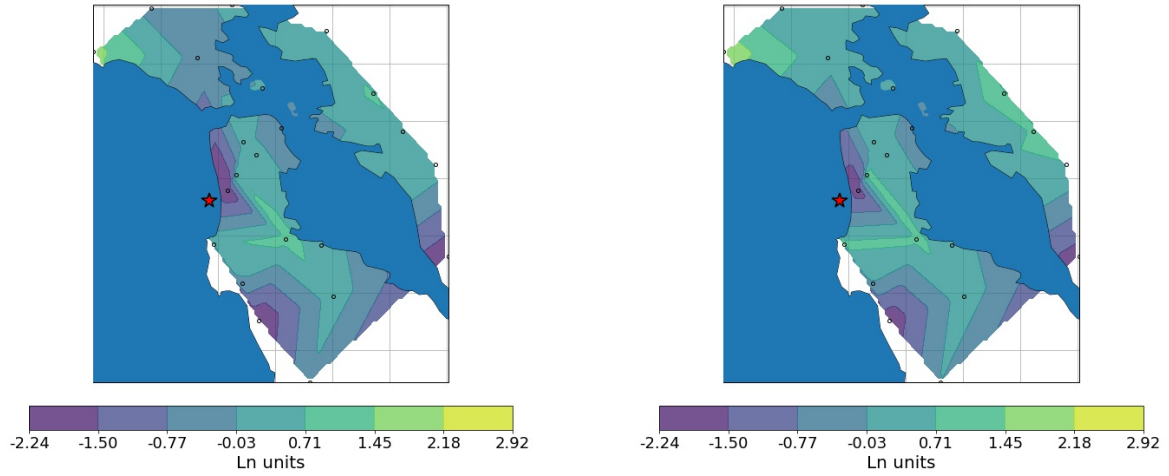
Figure 19: δW_{es} and radiation-pattern-corrected δW_{es} for the M4.0 August 17th, 2015 Piedmont earthquake at $T = 1$ s.



(a) Within-event residuals δW_{es}

(b) Radiation-pattern-corrected δW_{es}

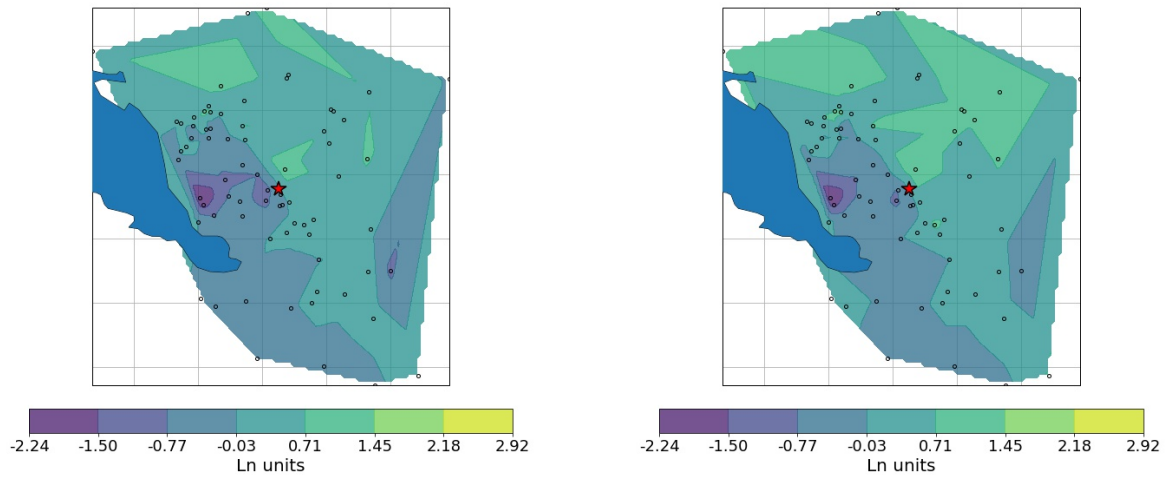
Figure 20: δW_{es} and radiation-pattern-corrected δW_{es} for the M4.9 May 13th, 2002 Gilroy earthquake at $T = 1$ s.



(a) Within-event residuals δW_{es}

(b) Radiation-pattern-corrected δW_{es}

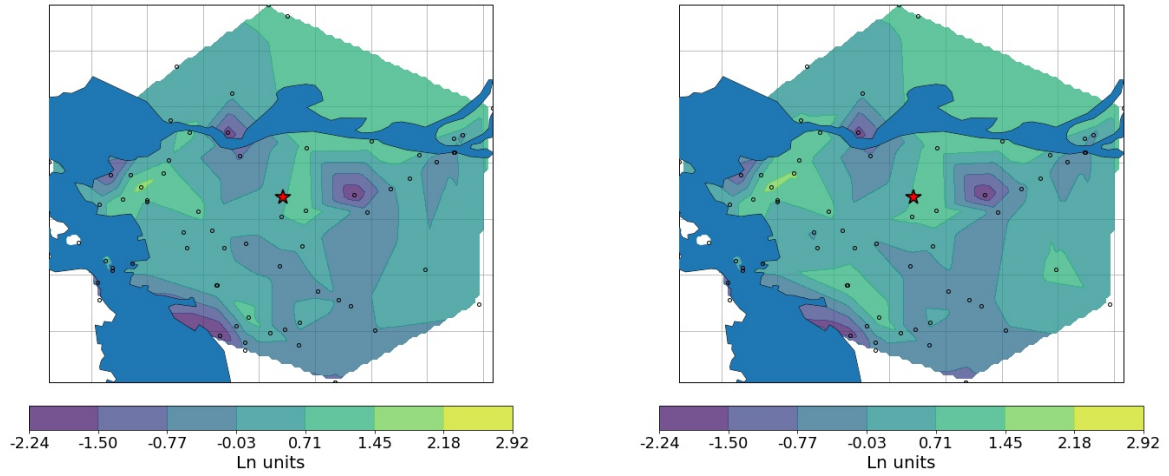
Figure 21: δW_{es} and radiation-pattern-corrected δW_{es} for the M3.5 October 5th, 2019 Colma earthquake at $T = 1$ s.



(a) Within-event residuals δW_{es}

(b) Radiation-pattern-corrected δW_{es}

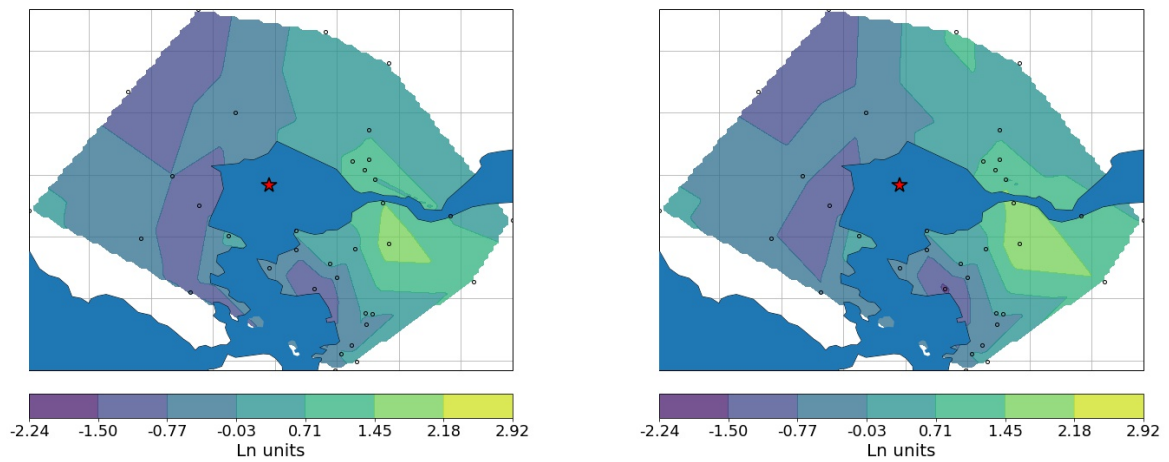
Figure 22: δW_{es} and radiation-pattern-corrected δW_{es} for the M4.0 July 21st, 2015 Fremont earthquake at $T = 1$ s.



(a) Within-event residuals δW_{es}

(b) Radiation-pattern-corrected δW_{es}

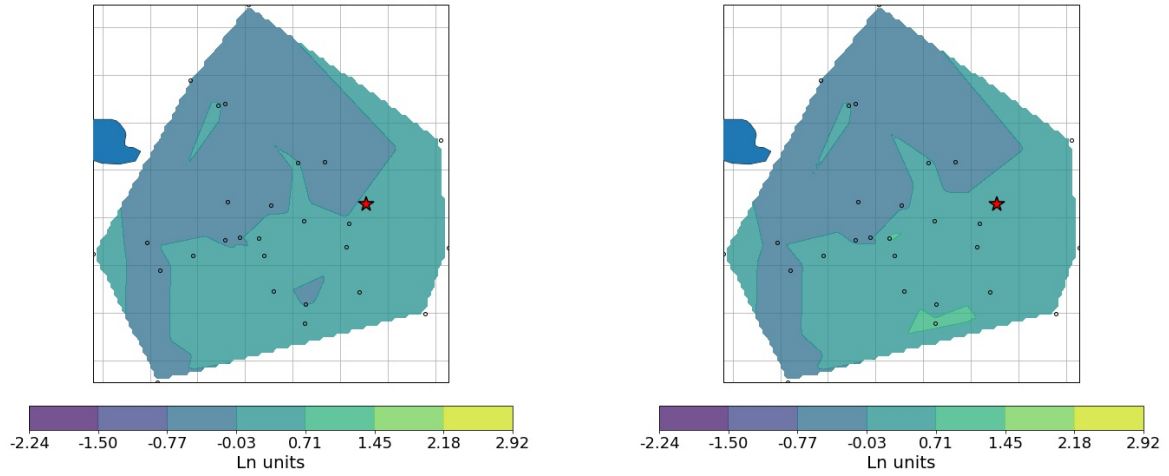
Figure 23: δW_{es} and radiation-pattern-corrected δW_{es} for the M4.5 October 14th, 2019 Pleasant Hill earthquake at $T = 1$ s.



(a) Within-event residuals δW_{es}

(b) Radiation-pattern-corrected δW_{es}

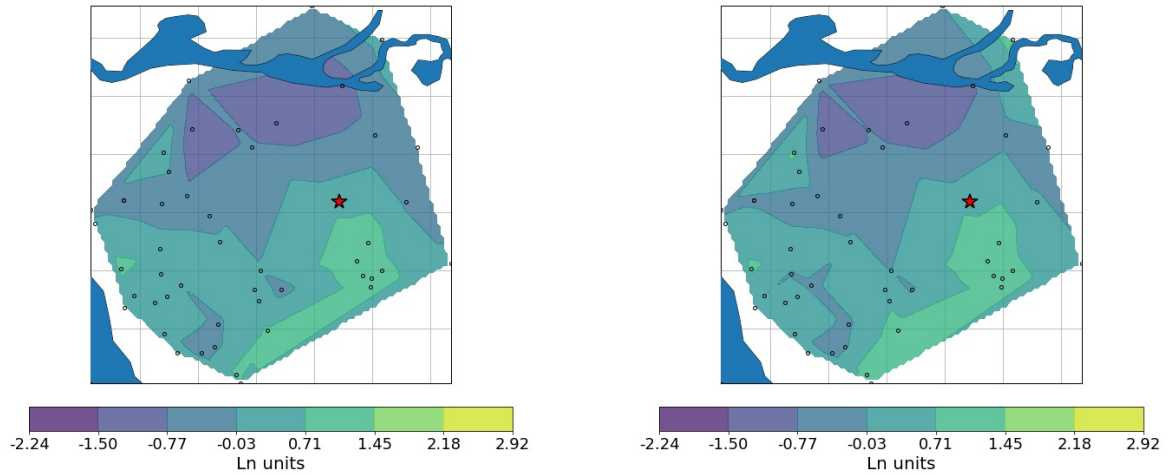
Figure 24: δW_{es} and radiation-pattern-corrected δW_{es} for the M3.5 November 10th, 2018 Crockett earthquake at $T = 1$ s.



(a) Within-event residuals δW_{es}

(b) Radiation-pattern-corrected δW_{es}

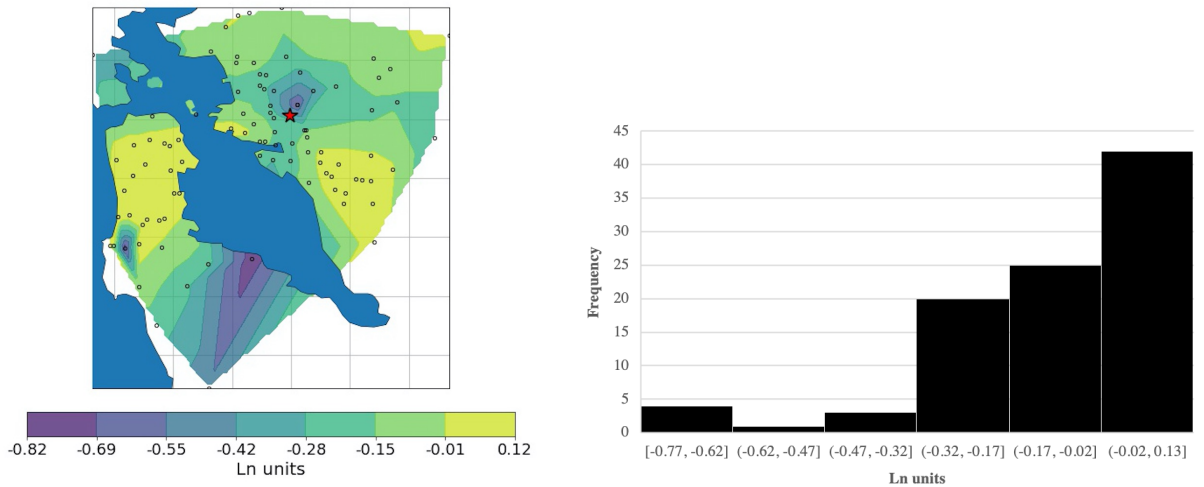
Figure 25: δW_{es} and radiation-pattern-corrected δW_{es} for the M3.9 December 26th, 2017 Alum Rock earthquake at $T = 1$ s.



(a) Within-event residuals δW_{es}

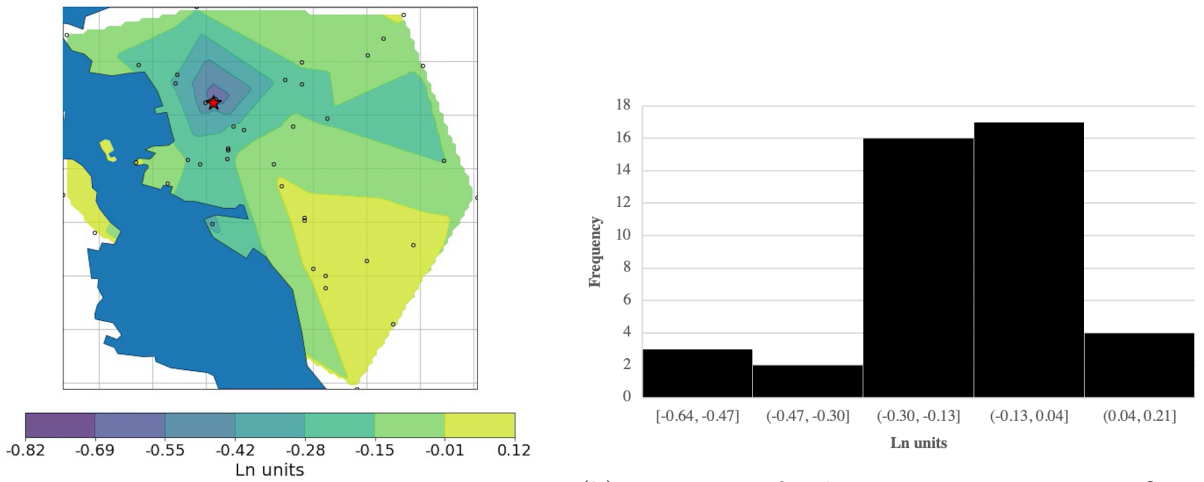
(b) Radiation-pattern-corrected δW_{es}

Figure 26: δW_{es} and radiation-pattern-corrected δW_{es} for the M4.3 July 16th, 2019 Byron earthquake at $T = 1$ s.



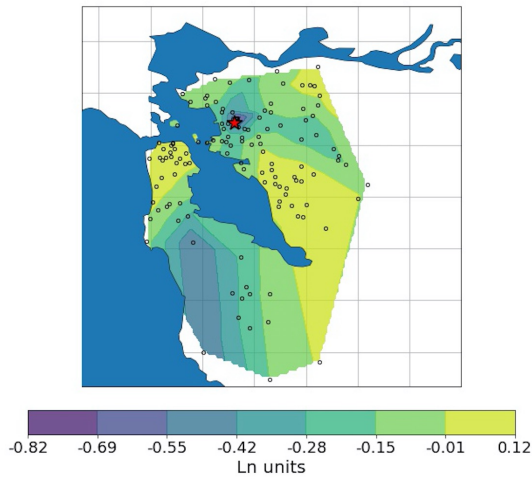
(a) Radiation pattern correction δW_{es} difference (b) Radiation pattern correction δW_{es} difference

Figure 27: The mapped distribution and histogram distribution of differences between δW_{es} and radiation-pattern-corrected δW_{es} for the M3.5 May 14th, 2018 Oakland earthquake at $T = 1$ s.

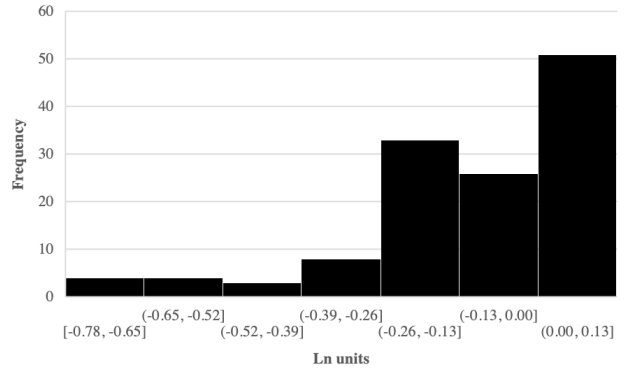


(a) Radiation pattern correction δW_{es} difference (b) Histogram of radiation pattern correction δW_{es} difference

Figure 28: The mapped distribution and histogram distribution of differences between δW_{es} and radiation-pattern-corrected δW_{es} for the M3.6 October 27th, 2011 Berkeley earthquake at $T = 1$ s.

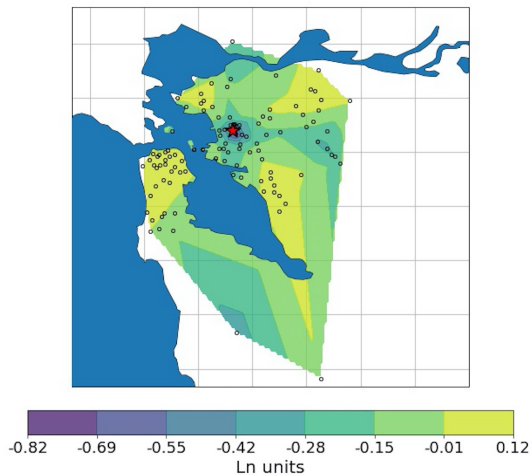


(a) Radiation pattern correction δW_{es} difference

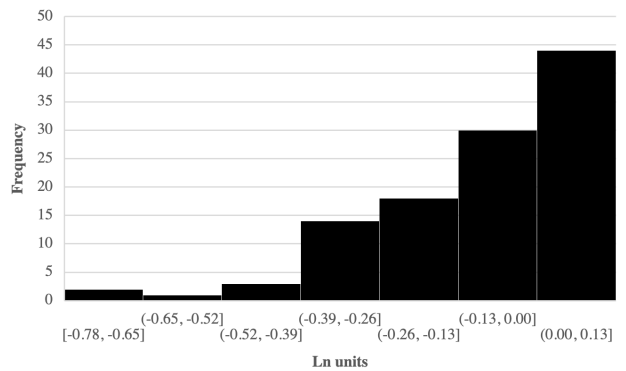


(b) Histogram of radiation pattern correction δW_{es} difference

Figure 29: The mapped distribution and histogram distribution of differences between δW_{es} and radiation-pattern-corrected δW_{es} for the M3.8 October 20th, 2011 Berkeley earthquake at $T = 1$ s.

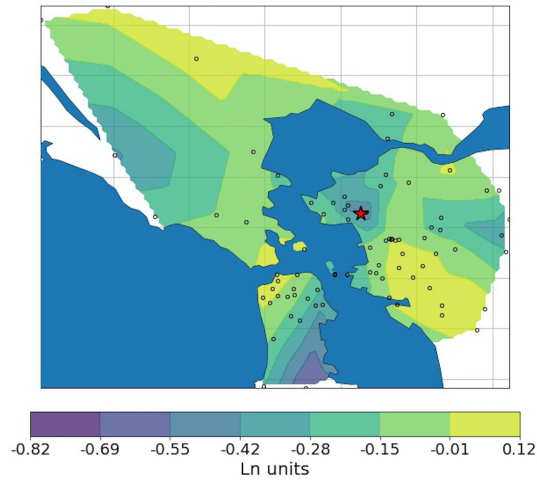


(a) Radiation pattern correction δW_{es} difference

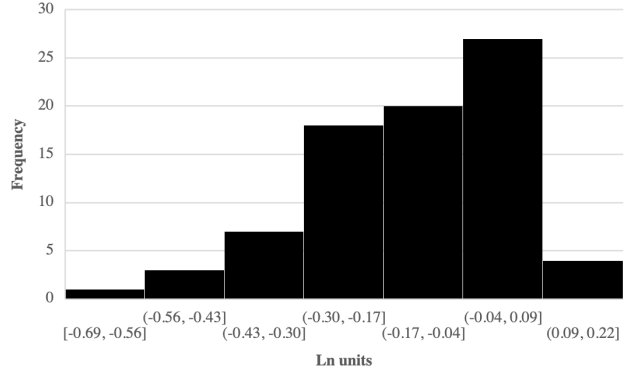


(b) Histogram of radiation pattern correction δW_{es} difference

Figure 30: The mapped distribution and histogram distribution of differences between δW_{es} and radiation-pattern-corrected δW_{es} for the M4.0 October 20th, 2011 Berkeley earthquake at $T = 1$ s.

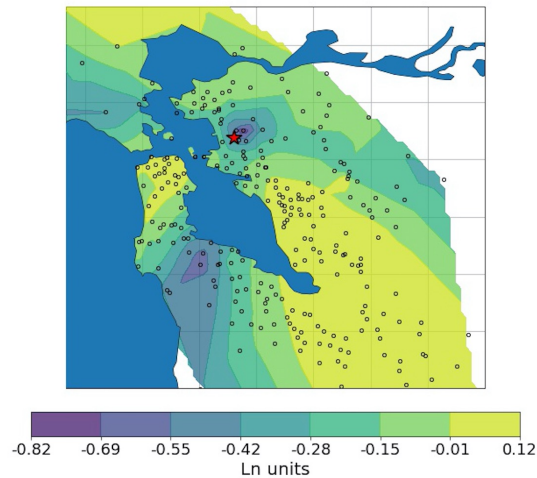


(a) Radiation pattern correction δW_{es} difference

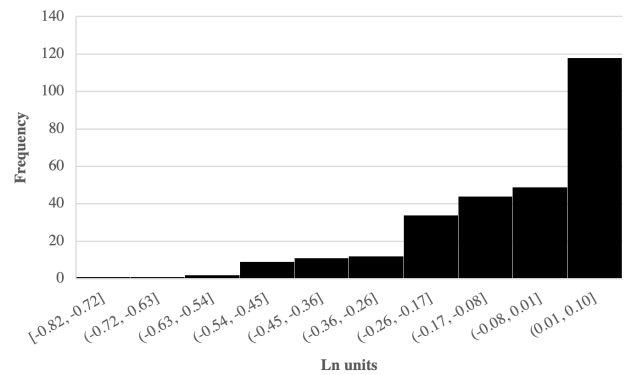


(b) Histogram of radiation pattern correction δW_{es} difference

Figure 31: The mapped distribution and histogram distribution of differences between δW_{es} and radiation-pattern-corrected δW_{es} for the M4.0 March 5th, 2012 El Cerrito earthquake at $T = 1$ s.

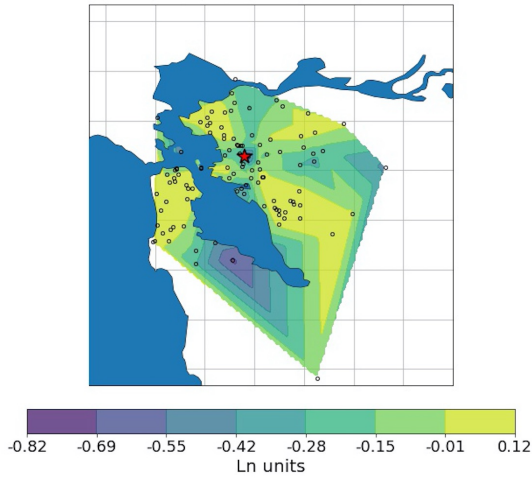


(a) Radiation pattern correction δW_{es} difference

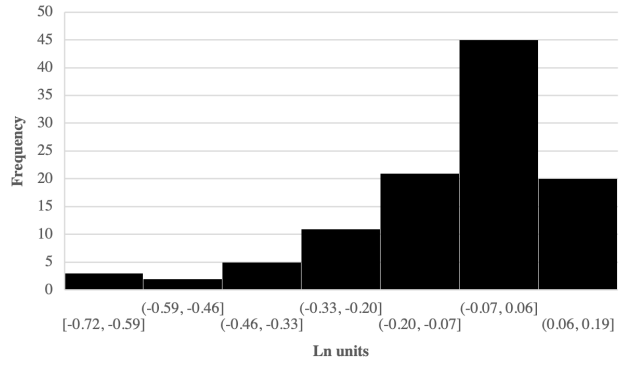


(b) Histogram of radiation pattern correction δW_{es} difference

Figure 32: The mapped distribution and histogram distribution of differences between δW_{es} and radiation-pattern-corrected δW_{es} for the M4.4 January 4th, 2018 Berkeley earthquake at $T = 1$ s.

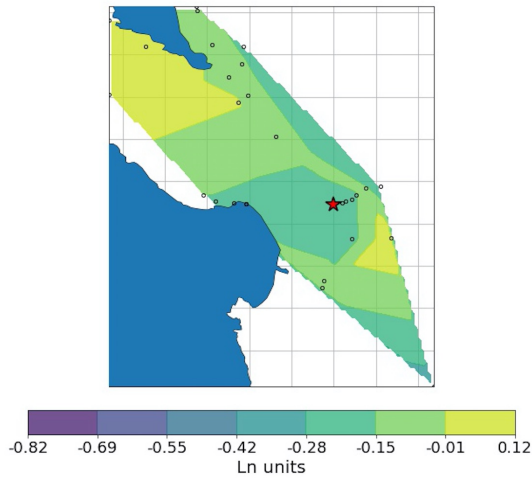


(a) Radiation pattern correction δW_{es} difference

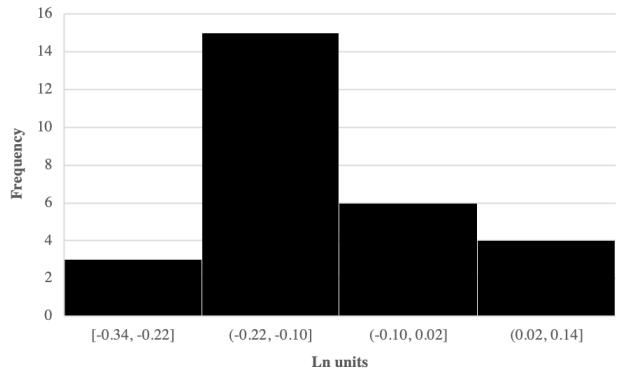


(b) Histogram of radiation pattern correction δW_{es} difference

Figure 33: The mapped distribution and histogram distribution of differences between δW_{es} and radiation-pattern-corrected δW_{es} for the M4.0 August 17th, 2015 Piedmont earthquake at $T = 1$ s.

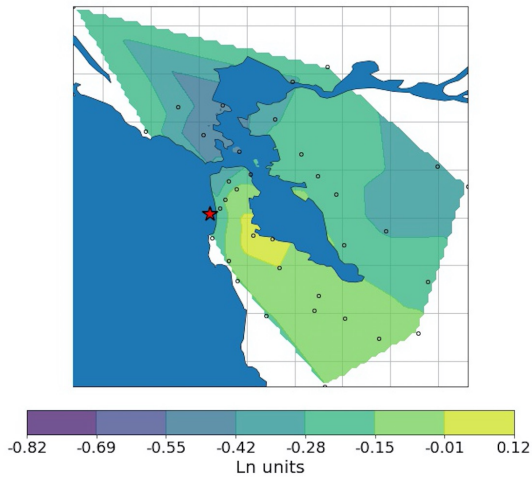


(a) Radiation pattern correction δW_{es} difference

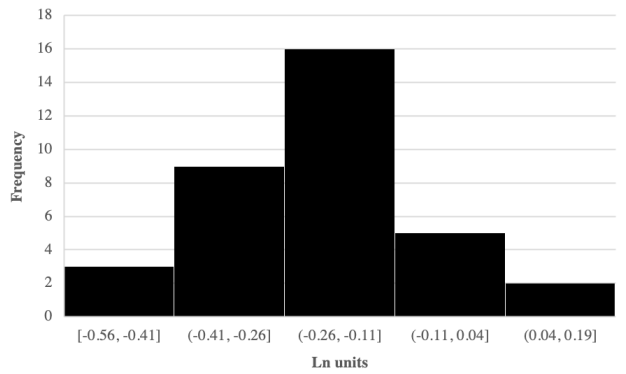


(b) Histogram of radiation pattern correction δW_{es} difference

Figure 34: The mapped distribution and histogram distribution of differences between δW_{es} and radiation-pattern-corrected δW_{es} for the M4.9 May 13th, 2002 Gilroy earthquake at $T = 1$ s.

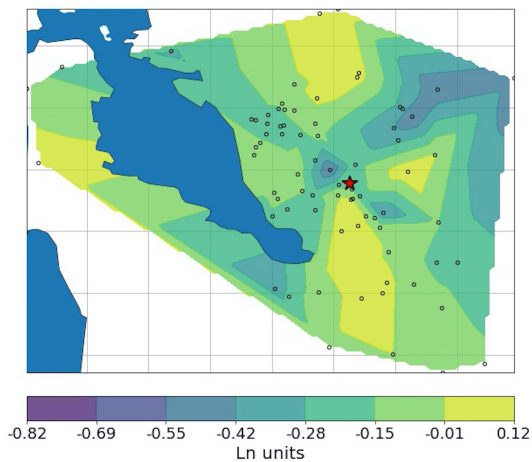


(a) Radiation pattern correction δW_{es} difference

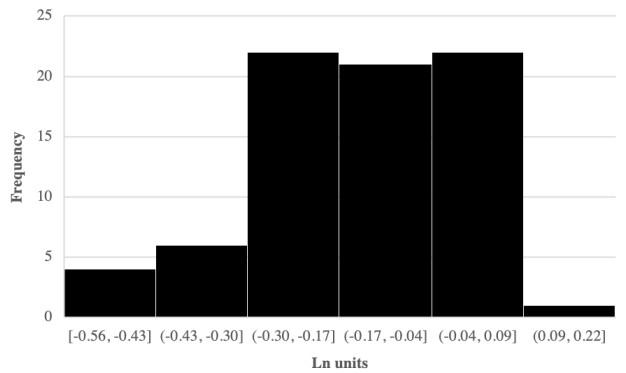


(b) Histogram of radiation pattern correction δW_{es} difference

Figure 35: The mapped distribution and histogram distribution of differences between δW_{es} and radiation-pattern-corrected δW_{es} for the M3.5 October 5th, 2019 Colma earthquake at $T = 1$ s.

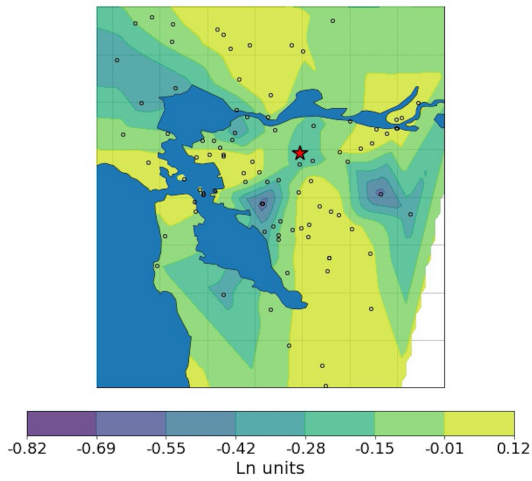


(a) Radiation pattern correction δW_{es} difference

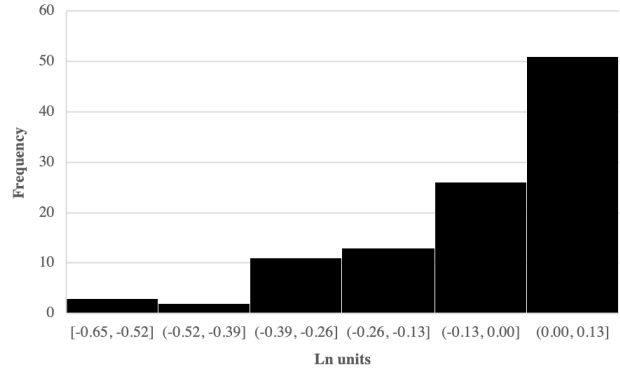


(b) Histogram of radiation pattern correction δW_{es} difference

Figure 36: The mapped distribution and histogram distribution of differences between δW_{es} and radiation-pattern-corrected δW_{es} for the M4.0 July 21st, 2015 Fremont earthquake at $T = 1$ s.

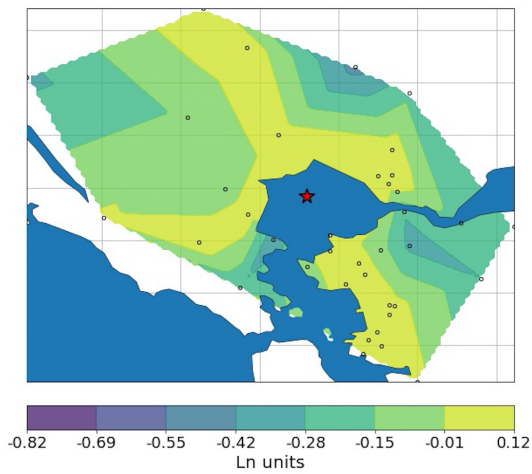


(a) Radiation pattern correction δW_{eS} difference

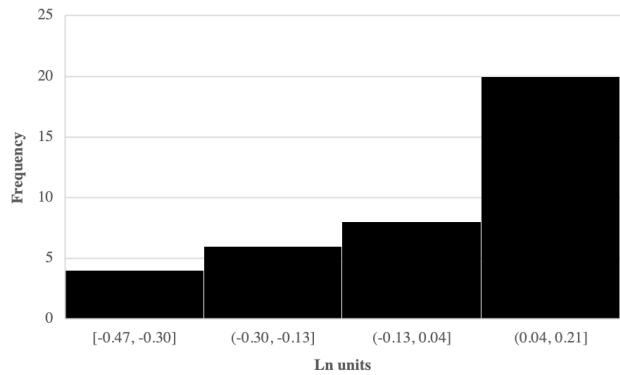


(b) Histogram of radiation pattern correction δW_{eS} difference

Figure 37: The mapped distribution and histogram distribution of differences between δW_{eS} and radiation-pattern-corrected δW_{eS} for the M4.5 October 14th, 2019 Pleasant Hill earthquake at $T = 1$ s.

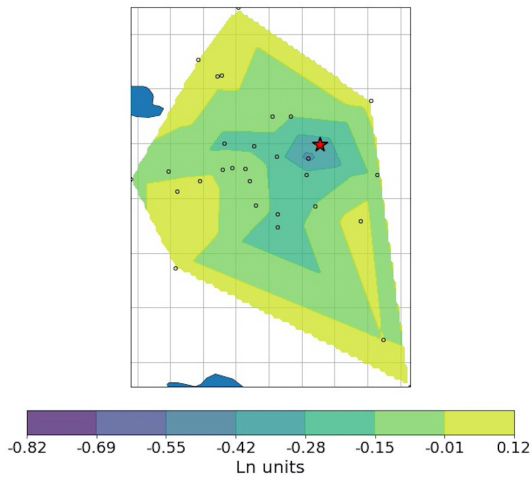


(a) Radiation pattern correction δW_{eS} difference

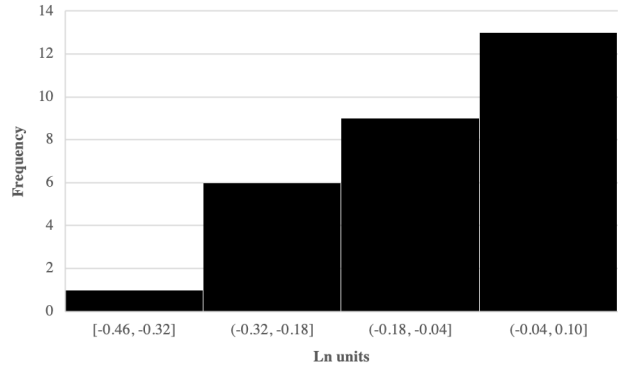


(b) Histogram of radiation pattern correction δW_{eS} difference

Figure 38: The mapped distribution and histogram distribution of differences between δW_{eS} and radiation-pattern-corrected δW_{eS} for the M3.5 November 10th, 2018 Crockett earthquake at $T = 1$ s.

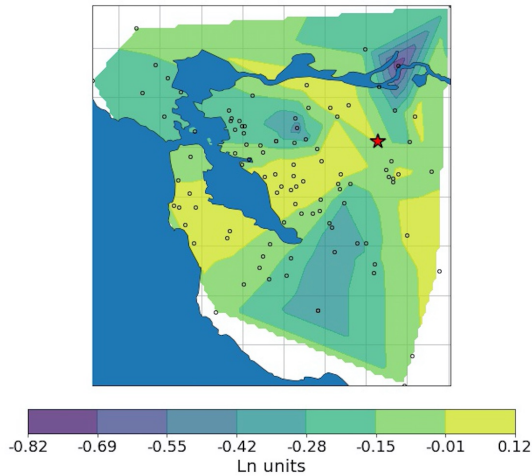


(a) Radiation pattern correction δW_{es} difference

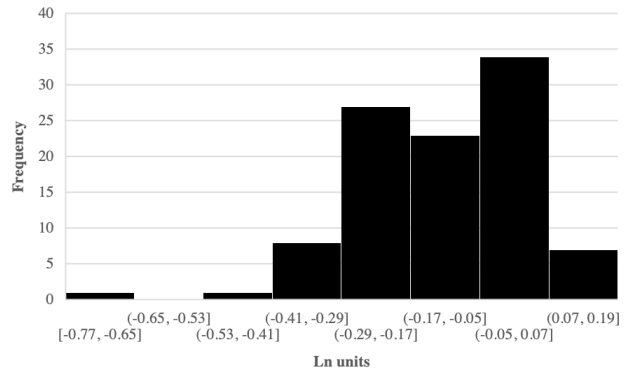


(b) Histogram of radiation pattern correction δW_{es} difference

Figure 39: The mapped distribution and histogram distribution of differences between δW_{es} and radiation-pattern-corrected δW_{es} for the M3.9 December 26th, 2017 Alum Rock earthquake at $T = 1$ s.

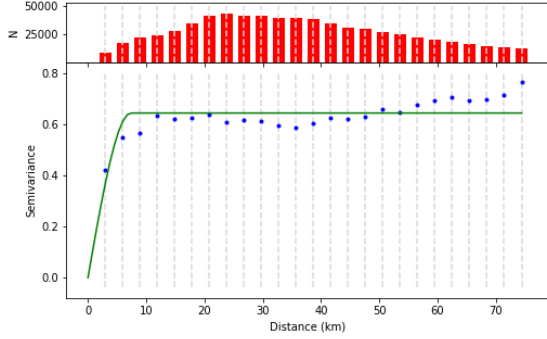


(a) Radiation pattern correction δW_{es} difference

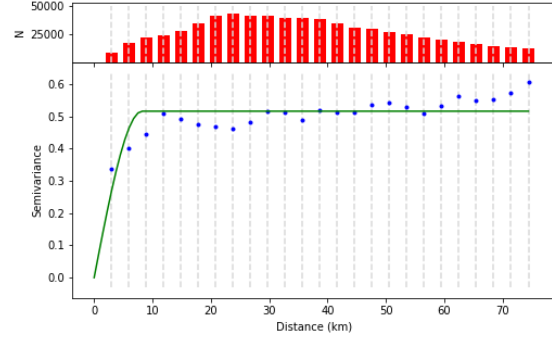


(b) Histogram of radiation pattern correction δW_{es} difference

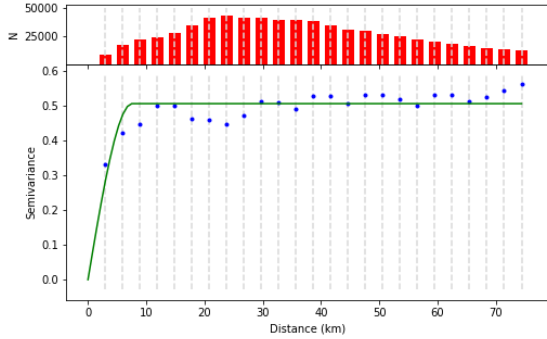
Figure 40: The mapped distribution and histogram distribution of differences between δW_{es} and radiation-pattern-corrected δW_{es} for the M4.3 July 16th, 2019 Byron earthquake at $T = 1$ s.



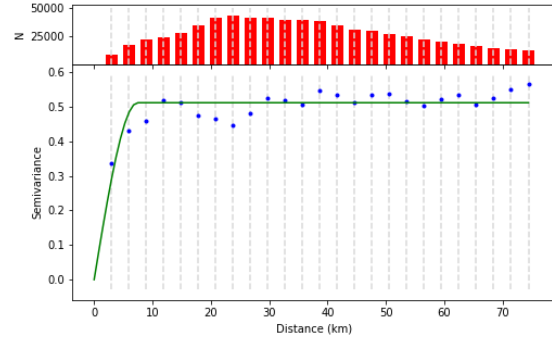
(a) $T = 0.2$ s



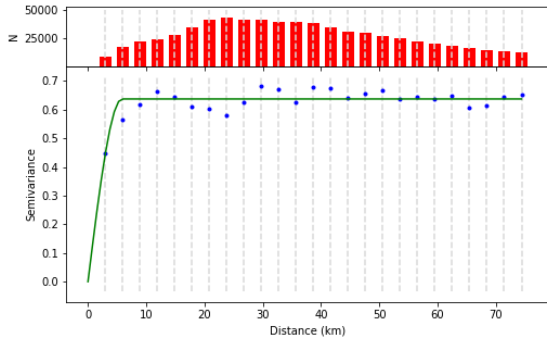
(b) $T = 0.5$ s



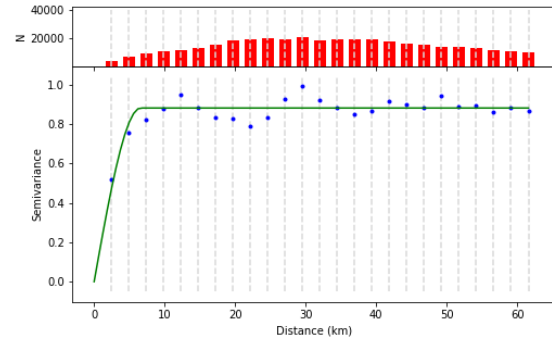
(c) $T = 0.75$ s



(d) $T = 1$ s

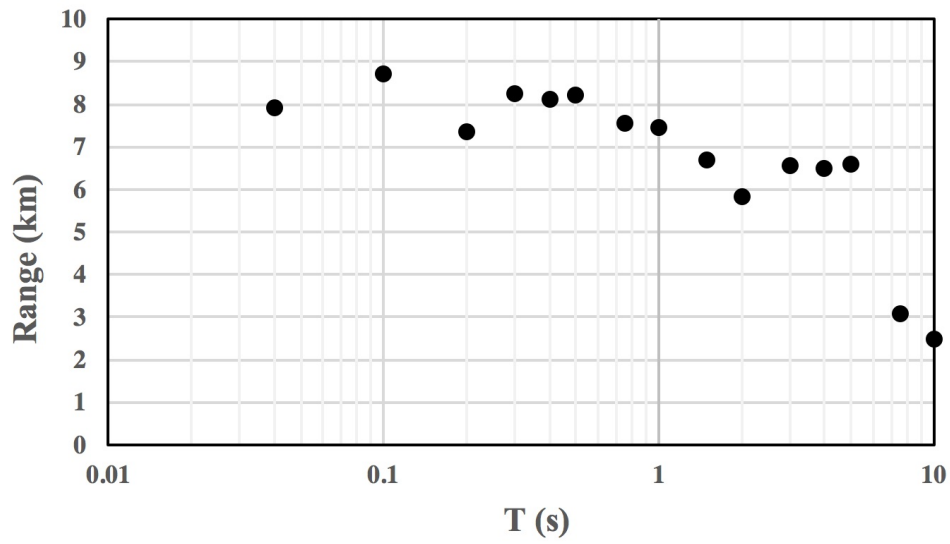


(e) $T = 2$ s

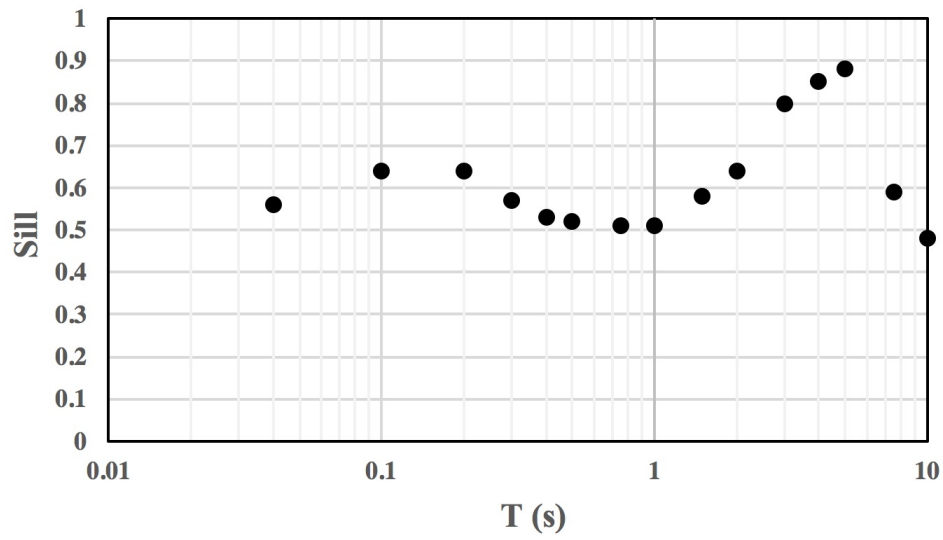


(f) $T = 5$ s

Figure 41: Semivariogram of within-event residuals δW_{es} at $T = 0.2$ s, 0.5 s, 0.75 s, 1 s, 2 s, and 5 s.



(a) Period T (s) dependence of range (km)



(b) Period T (s) dependence of sill

Figure 42: Semivariogram values by period T (s).

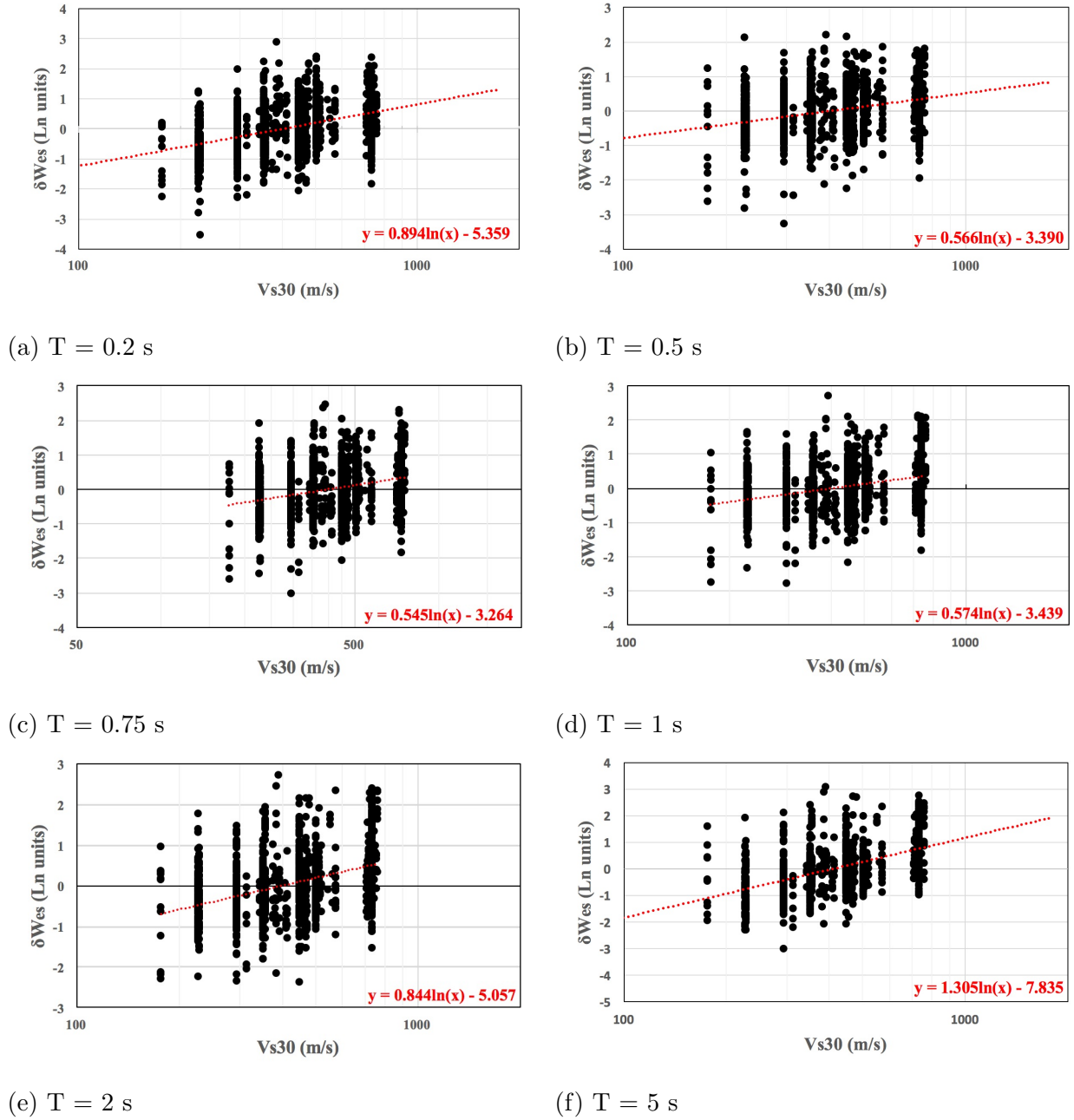


Figure 43: V_{S30} dependence of within-event residuals δW_{es} at $T = 0.2$ s, 0.5 s, 0.75 s, 1 s, 2 s, and 5 s in logarithm units.

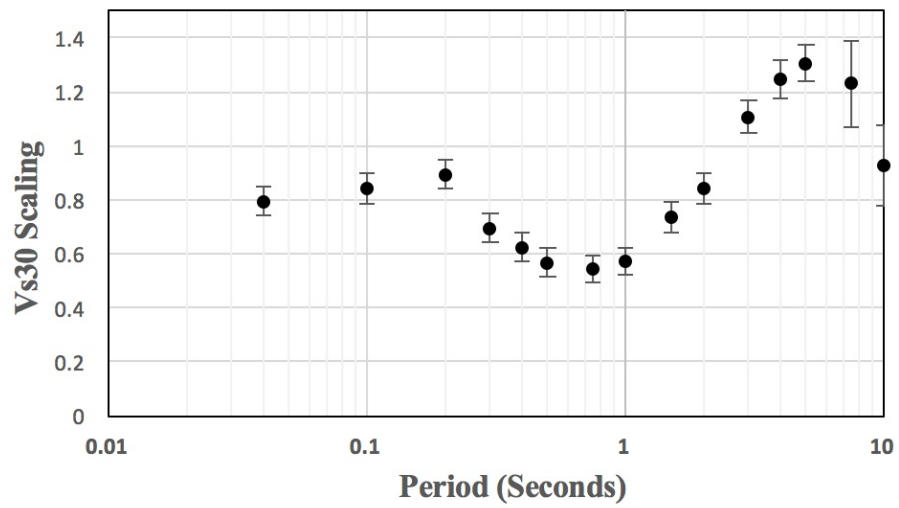
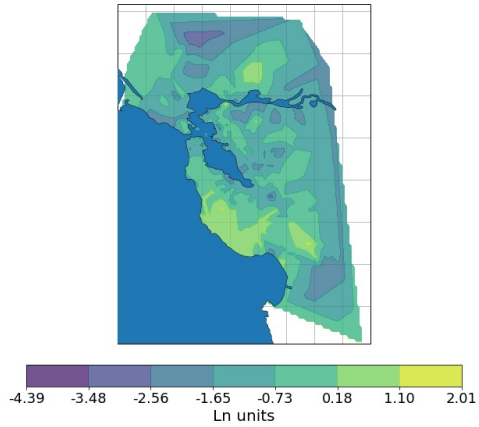
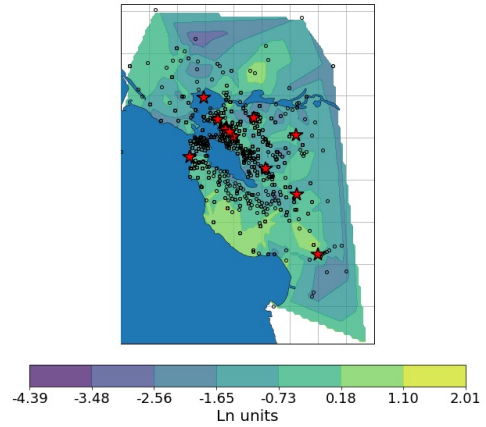


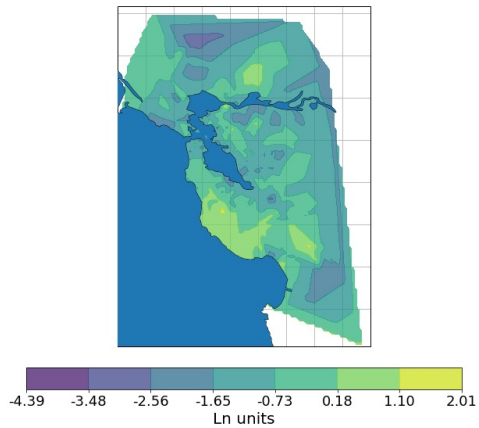
Figure 44: δW_{es} and radiation-pattern-corrected δW_{es} for the M3.6 October 27th, 2011 Berkeley earthquake at $T = 1$ s.



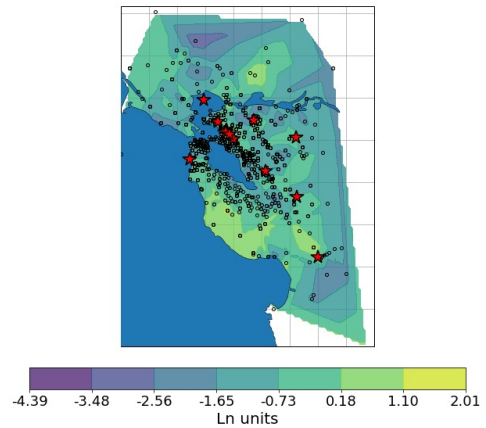
(a) Velocity-corrected δW_{es}



(b) Velocity-corrected δW_{es}

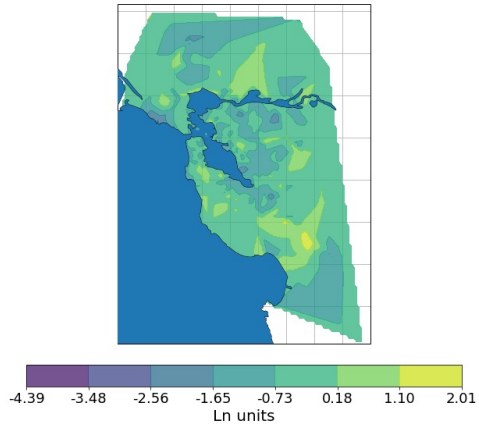


(c) Velocity-corrected and radiation-pattern-corrected δW_{es}

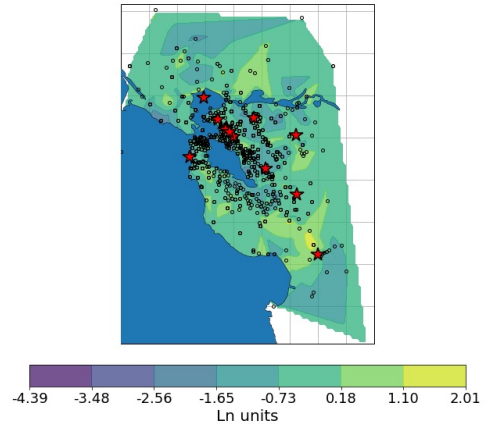


(d) Velocity-corrected and radiation-pattern-corrected δW_{es}

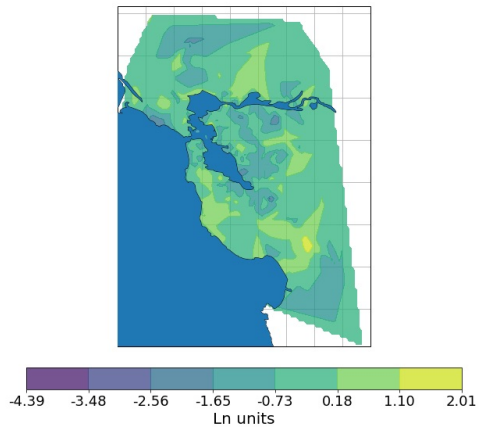
Figure 45: Velocity-corrected δW_{es} and both velocity-corrected and radiation-pattern-corrected δW_{es} for all earthquakes at $T = 0.2$ s.



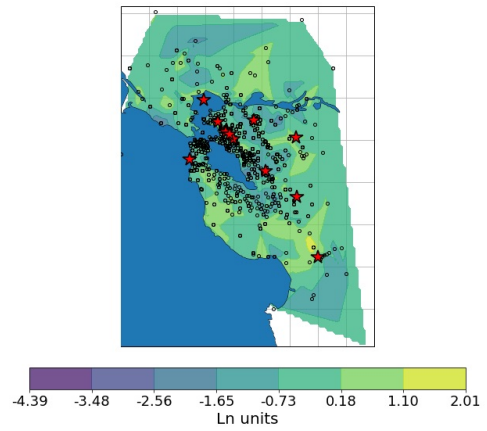
(a) Velocity-corrected δW_{es}



(b) Velocity-corrected δW_{es}

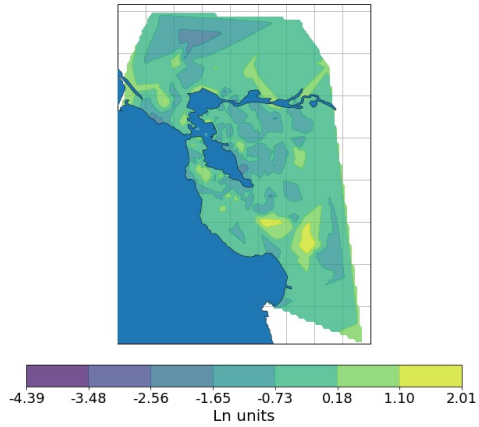


(c) Velocity-corrected and radiation-pattern-corrected δW_{es}

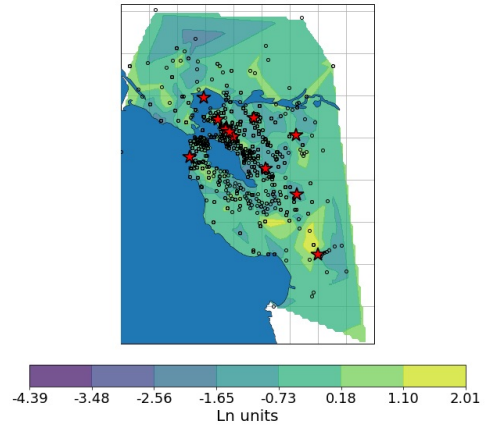


(d) Velocity-corrected and radiation-pattern-corrected δW_{es}

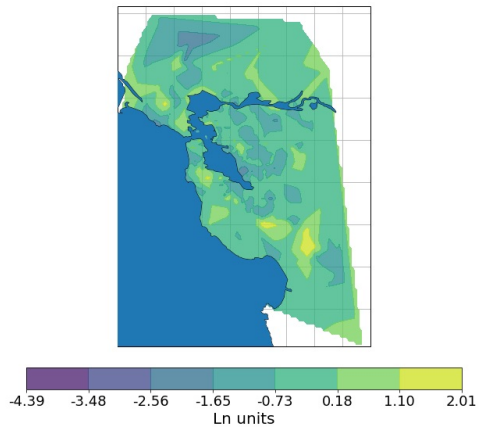
Figure 46: Velocity-corrected δW_{es} and both velocity-corrected and radiation-pattern-corrected δW_{es} for all earthquakes at $T = 0.5$ s.



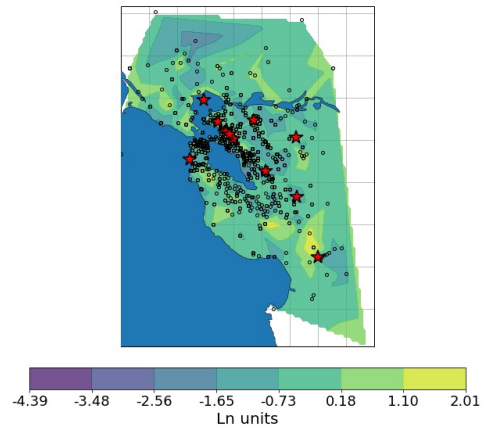
(a) Velocity-corrected δW_{es}



(b) Velocity-corrected δW_{es}

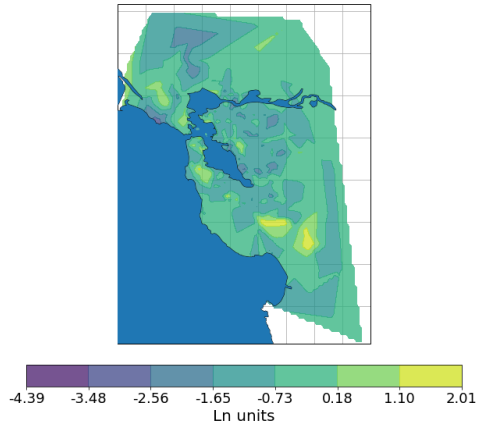


(c) Velocity-corrected and radiation-pattern-corrected δW_{es}

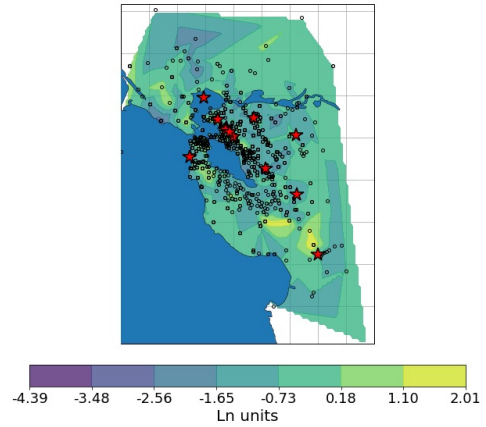


(d) Velocity-corrected and radiation-pattern-corrected δW_{es}

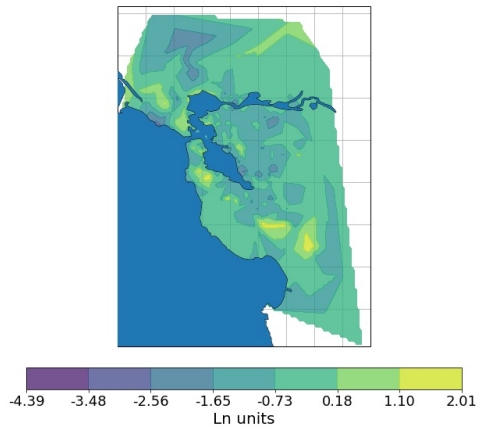
Figure 47: Velocity-corrected δW_{es} and both velocity-corrected and radiation-pattern-corrected δW_{es} for all earthquakes at $T = 1$ s.



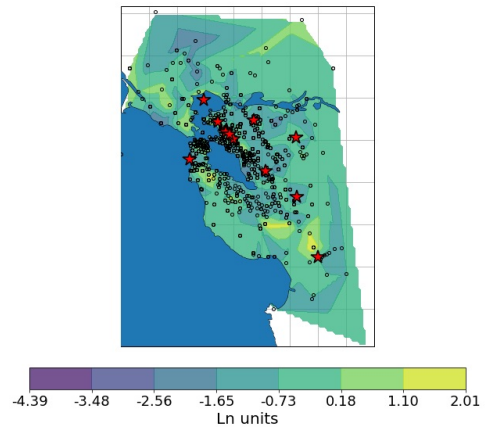
(a) Velocity-corrected δW_{es}



(b) Velocity-corrected δW_{es}

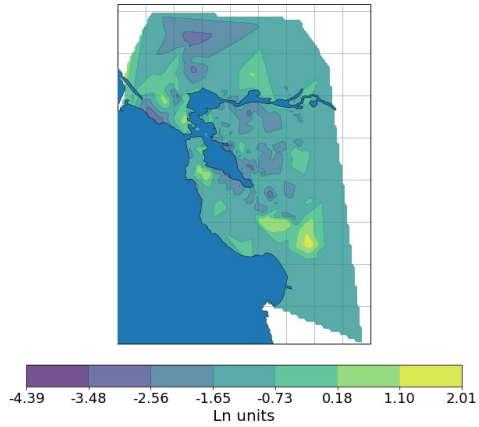


(c) Velocity-corrected and radiation-pattern-corrected δW_{es}

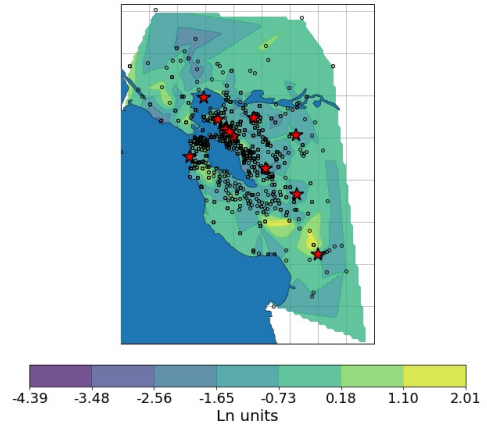


(d) Velocity-corrected and radiation-pattern-corrected δW_{es}

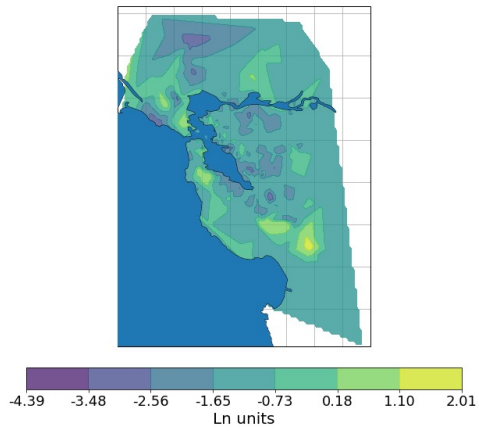
Figure 48: Velocity-corrected δW_{es} and both velocity-corrected and radiation-pattern-corrected δW_{es} for all earthquakes at $T = 2$ s.



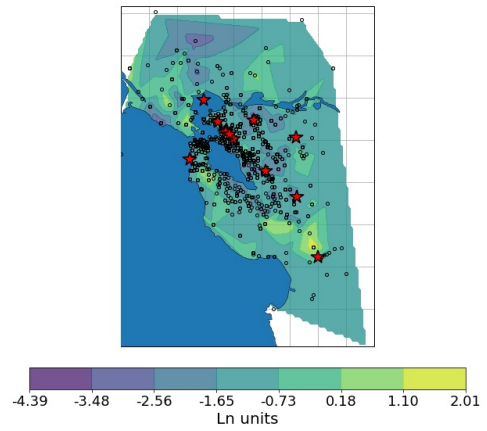
(a) Velocity-corrected δW_{es}



(b) Velocity-corrected δW_{es}



(c) Velocity-corrected and radiation-pattern-corrected δW_{es}



(d) Velocity-corrected and radiation-pattern-corrected δW_{es}

Figure 49: Velocity-corrected δW_{es} and both velocity-corrected and radiation-pattern-corrected δW_{es} for all earthquakes at $T = 5$ s.

Tables

Table 1: Moderate-magnitude Bay Area earthquakes

Magnitude	Location	Date	Epicenter
3.5	Oakland	05/14/2018	37.805, -122.202
3.6	Berkeley	10/27/2011	37.873, -122.251
3.8	Berkeley	10/20/2011	37.869, -122.252
4.0	Berkeley	10/20/2011	37.864, -122.250
4.0	El Cerrito	03/05/2012	37.929, -122.304
4.4	Berkeley	01/04/2018	37.856, -122.257
4.0	Piedmont	08/17/2015	37.837, -122.232
4.9	Gilroy	05/13/2002	36.967, -121.600
3.5	Colma	10/05/2019	37.660, -122.515
4.0	Fremont	07/21/2015	37.5772, -121.974
4.5	Pleasant Hill	10/14/2019	37.938, -122.057
3.5	Crockett	11/10/2018	38.083, -122.410
3.9	Alum Rock	12/26/2017	37.397, -121.747
4.3	Byron	07/16/2019	37.819, -121.757

Table 2: Periodic radiation pattern S_1 , standard error, and t ratio

T(s)	S_1	Standard Error	t Ratio
0.04	0.027	0.164	0.16
0.1	0.137	0.176	0.78
0.2	0.265	0.176	1.50
0.3	0.745	0.166	4.50
0.4	0.836	0.158	5.28
0.5	1.017	0.156	6.51
0.75	1.193	0.155	7.68
1	1.287	0.156	8.23
1.5	1.276	0.167	7.65
2	1.210	0.175	6.93
3	1.061	0.195	5.44
4	0.907	0.233	3.89
5	0.838	0.238	3.53
7.5	1.177	0.629	1.87
10	1.042	0.566	1.84

Table 3: Periodic range and sill values

T(s)	Range (km)	Sill
0.04	7.92	0.56
0.1	8.73	0.64
0.2	7.37	0.64
0.3	8.24	0.57
0.4	8.13	0.53
0.5	8.22	0.52
0.75	7.57	0.51
1	7.44	0.51
1.5	6.68	0.58
2	5.82	0.64
3	6.55	0.80
4	6.51	0.85
5	6.58	0.88
7.5	3.08	0.59
10	2.49	0.48

Table 4: Periodic V_{S30} scaling

T(s)	V_{S30} scaling	Standard Error
0.04	0.795	0.054
0.1	0.841	0.056
0.2	0.894	0.055
0.3	0.695	0.054
0.4	0.622	0.053
0.5	0.566	0.053
0.75	0.545	0.051
1	0.574	0.051
1.5	0.735	0.055
2	0.844	0.056
3	1.105	0.060
4	1.246	0.069
5	1.305	0.069
7.5	1.230	0.160
10	0.928	0.148